

## Article

# Implementation of Data from Wind Tunnel Tests in the Design of a Tall Building with an Elliptic Ground Plan

Ol'ga Hubová <sup>1</sup>, Marek Macák <sup>2</sup>, Michal Franek <sup>1</sup>, Ol'ga Ivánková <sup>3,\*</sup> and Lenka Bujdáková Konečná <sup>4</sup>

<sup>1</sup> Department of Building Construction, Faculty of Civil Engineering, Slovak University of Technology in Bratislava, Radlinského 11, SK-810 05 Bratislava, Slovakia; olga.hubova@stuba.sk (O.H.); michal.franek@stuba.sk (M.F.)

<sup>2</sup> Department of Mathematics and Descriptive Geometry, Faculty of Civil Engineering, Slovak University of Technology in Bratislava, Radlinského 11, SK-810 05 Bratislava, Slovakia; marek.macak@stuba.sk

<sup>3</sup> Department of Structural Mechanics, Faculty of Civil Engineering, Slovak University of Technology in Bratislava, Radlinského 11, SK-810 05 Bratislava, Slovakia

<sup>4</sup> Secondary Industrial School of Construction and Surveyor, Drieňová 35, SK-526 64 Bratislava, Slovakia; ing.konecna@gmail.com

\* Correspondence: olga.ivankova@stuba.sk

**Abstract:** The design of a 69 m tall multipurpose building was investigated in this paper. The shape of the structure above the ground was an elliptical cylinder. Under the ground, the building was extended into a cuboid shape (for car parking). External wind pressure coefficients were determined using three methods: wind tunnel tests, CFD, and “the simplification of the shape” (using information defined in building standards). From the obtained results, it was evident that the simplification did not provide results with sufficient accuracy. The external wind pressure coefficients presented in this paper should be used for the design of a similar structure. The shape of the elliptical cylinder is very sensitive to applied wind. Positive pressures only occur on a small area of the windward side. The rest of the windward side is loaded with negative pressures. Therefore, torsional effects can occur, and these can be dangerous for the structure. The leeward side is completely loaded with negative pressures. In our case, this information was necessary for a follow-on static and dynamic analysis of the building. Various subsoil stiffness coefficients were considered. The calculated horizontal displacement was compared with the limit value. A measured wind direction of 20° caused the maximum obtained torsional moment, and a wind direction of 90° induced the maximum obtained force. The commercial program Ansys Fluent 2022 was used for the CFD simulation. The SCIA ENGINEER 21 program was used for follow-on analysis. This paper presents brief information on the selected turbulence model and details the settings used for the CFD simulation. Also, a description of the wind tunnel laboratory utilized in this study is provided, along with a description of the measuring devices used and the methodologies of the tests carried out. The main purpose of this paper is to show how important it is to consider the wind load for the static analysis of a structure like this.

**Keywords:** tall building; external pressure coefficients; experimental measurements; boundary layer wind tunnel; computational fluid dynamics; static analysis; elliptical cylinder



**Citation:** Hubová, O.; Macák, M.; Franek, M.; Ivánková, O.; Konečná, L.B. Implementation of Data from Wind Tunnel Tests in the Design of a Tall Building with an Elliptic Ground Plan. *Buildings* **2023**, *13*, 2732. <https://doi.org/10.3390/buildings13112732>

Academic Editor: Theodore Stathopoulos

Received: 3 September 2023

Revised: 9 October 2023

Accepted: 16 October 2023

Published: 29 October 2023



**Copyright:** © 2023 by the authors. Licensee MDPI, Basel, Switzerland. This article is an open access article distributed under the terms and conditions of the Creative Commons Attribution (CC BY) license (<https://creativecommons.org/licenses/by/4.0/>).

## 1. Introduction

This paper was inspired by real structures that were built in Bratislava (the capital city of Slovakia) in recent years (see Figure 1). These buildings look, very simply, elegant; they are among the most beautiful buildings in Bratislava [1–3]. There are many similar buildings all over the world, but these are taller. They are characteristic of the architecture of the 21st century, possessing the following features: tube structure; materials—glass, steel, aluminum, and concrete; the cladding comprises large glass panels; the total shape of the

structure is either symmetrical or entirely asymmetrical. In this case study, as shown in Figure 1, the buildings have one common feature—they have an elliptical cylindrical shape.



(a)



(b)



(c)



(d)

**Figure 1.** Tall buildings with elliptic ground plan in Bratislava: (a) three towers (for more information, visit [1]); (b) headquarters of VUB bank; (c) national football stadium (for more information, visit [2]); (d) SKY PARK designed by Zaha Hadid.

Elliptical cylinders appear to be a very easy shape to create, but the problem lies in determining the wind pressure distribution, accounting for the influence of the vortices that are generated (this shape is not mentioned in the building standards). Therefore, the elliptical shape has been investigated by several researchers. A comparison between the five basic shapes of buildings (square, triangular, rectangular, circular, and elliptical) is presented in [4]. The data from wind tunnel tests were compared with values defined by the National Building Code of Canada and the American Society of Civil Engineers. A very important takeaway from this research is that elliptical-, triangular-, and rectangular-shaped buildings are more sensitive to high torsion loading, which is induced by wind applied to the structure. This fact was also confirmed by the results of our research (see Section 3).

A comprehensive study of tall buildings with elliptical cross-sections, using CFD simulation, is presented in [5]. The proportions of the cross-section (the length and the width expressed by the cross-sectional aspect ratio) were changed. Different wind directions and levels were measured and investigated. The aim was to predict the surface wind pressure distribution and its uses for natural ventilation in the interior spaces of tall buildings.

The shape of a whole structure is very important in determining the structure's response to wind. When wind is applied to a structure and the shape of the structure is not aerodynamic, the horizontal displacements could be too large. Therefore, the selection or optimization of a shape is an important part of the design of the structure—especially in the case of tall (up to 100 m), high-rise (100–150 m), skyscraper (150–300 m), supertall (300–600 m) and megatall buildings (higher than 600 m). It is mentioned in [6] that the stiffness of the structural system affects the vertical deflection and horizontal displacements of a building. Horizontal displacements depend on the value of wind load and also on the aerodynamic properties of a building. Wind load increases with the height of a structure. A high spatial stiffness of a building reduces the horizontal displacements but leads to a lower eigenfrequency of the structure. This can be dangerous for the structure because of the resonance at critical wind speeds (high stresses and vertical deflection will be generated).

Wind effects around an elliptical cylinder placed near a flat plate were experimentally investigated in [7]. The distance between both elements was changed, and wind pressure distribution on their surfaces was measured. The investigation of the elliptic shape by tests performed in a water channel is described in [8]. The authors tried to estimate the creation of vortices in dependence on the height of submergence in the water channel. Due to its significance in civil engineering design, the bluff body's flow has been widely investigated. Therefore, let us focus only on the elliptical cylinder. A detailed study of a stationary elliptical cylinder was presented by Modi and Wiland [9]. The variation of the Strouhal  $St$  number with the Reynolds number  $Re$ , the mean and fluctuating static pressure distribution, and wake geometry were experimentally tested. There were a few suggestions for future investigation: the  $Re$  effect at zero angle of attack, the separation point, etc. Wakes behind elliptical cylinders developed secondary shear layer instabilities further downstream, representing unequal wake frequencies that destroy the wake's periodicity. An analytical investigation of wake and streamline patterns for a low  $Re$  was performed [10–12]. Thompson et al. [12] documented the Strouhal number and drag coefficient variations with Reynolds number for the two-dimensional shedding regime with various aspect ratios of an elliptical cylinder.

When the wind changes suddenly (as in the case of strong wind gusts), large inertia forces in a structure in the tangential and radial directions are induced. This has a negative influence on the structure. The study [13] is focused on the overshoot phenomenon. It is the cause of larger wind forces in comparison with a steady flow (this occurs on a structure subjected to short-rise time gusts). The unsteady wind force applied to the structure was rapidly changed from a steady flow. The wind gusts were modeled in a wind tunnel using the following parameters: target wind velocity was in the range of 2.0–7.0 m/s, initial wind velocity was from 0.0 to 0.9 m/s, and rise time was between 0.1 and 1.4 s.

The topic of [14] is the wake stability of elliptical cylinders. Varied angles of flow direction ( $0^\circ$ – $30^\circ$ ) and different dimensions of the cylinder with a Reynolds number of more than 500 were considered.

Another paper devoted to aerodynamic shape optimization by using CFD simulation is [15]. The original shape of the cross-section—rectangular—was slightly modified by an ellipse in both directions. The aim was to reduce the wind-induced loads on the structures by using double-skin facades. Different wind directions ( $0$ – $90^\circ$ ) were considered.

An elliptical cylinder with a varied cross-sectional aspect ratio (the proportion of minor axis to major axis) was numerically analyzed by using a 2D CFD simulation in the program Ansys Fluent [16]. The wind direction was changed in the range of 0–90°. Three different flow patterns on the leeward side were observed and described. This information can be useful for the prediction of the effects of wind on pedestrians passing around buildings with an elliptic ground plan.

The static and dynamic analysis of tall buildings with varied heights (from 17.5 m to 105 m) is described in [17]. Three different methods for the calculation of static and dynamic displacements are compared, and the recommendations for civil engineers are specified.

The main purpose of this paper is to show how important it is to consider the wind load for the static analysis of a structure like this. The authors' results and conclusions can help the construction practice and give methodological instructions for evaluating the wind loads on a cylinder with an elliptic ground plan.

## 2. Description of the Building

A multipurpose 21-story building located in flat urban terrain in Bratislava (the capital city of Slovakia) was analyzed. The shape of the building above the ground was an elliptical cylinder with a height of 67.95 m. Under the ground, the building was extended to a cuboid with a height of 10.5 m (three stories) (Figure 2a). The utilization of the building was as follows: all three underground floors (Figure 2c)—parking spots; 1st floor—commercial spaces; from 2nd to 20th floor—residential function; 21st floor—technical floor. The roof of the building was ended by a 1 m high roof parapet. The roof was designed without utilization. The dimensions of the ground plan of a typical floor are depicted in Figure 2d. The structural height was different according to the utilization of the floor: all underground floors—3.5 m; 1st floor—3.95 m; from 2nd to 21st floor—3.2 m. This paper was inspired by the real structure, where reinforced concrete walls were coupled with one big stiffening core in the middle of the building. We did not want to make a copy of the structural system used in the case of the real structure; therefore, two small stiffening cores were considered. The structural system was designed with respect to the limit values of the horizontal and vertical displacements defined in the standards and according to recommendations mentioned in [18–20]. It was created step-by-step. Firstly, only reinforced columns and stiffening walls in the middle of the ground plan were designed. Horizontal displacements were too large, and other stiffening walls had to be added. The resultant structural system is shown in Figure 2b. The maximum span between the vertical structural elements was 6 m in both directions. The cross-sectional aspect ratio of the elliptical cylinder was 0.4 (the ratio of minor axis to major axis), as shown in Figure 2d.

The dimensions of all horizontal and vertical structural elements were determined by preliminary calculations. The thicknesses of plane elements were as follows: foundation slab—1800 mm; horizontal slabs—250 mm; all interior stiffening walls—400 mm; outer underground walls—350 mm; roof parapet—250 mm. Circular reinforced concrete columns were considered in the whole building, but their diameter was changed with respect to the height of the building. Underground section:  $\varnothing$  800 mm under the elliptical cylinder; others,  $\varnothing$  600 mm. Upper part:  $\varnothing$  800 mm up to 2nd floor,  $\varnothing$  600 mm from 3rd to 12th floor,  $\varnothing$  600 mm from 13th to 21st floor. All elliptical slabs were enclosed by girders with the dimensions of 350 mm  $\times$  600 mm. Light external cladding (aluminum frame with triple insulating glass) with a weight of 100 kg/m<sup>2</sup> was applied on the whole building.

All structural elements were made of reinforced concrete (concrete C 30/37, steel B500B). The 3D model of the structure was created in the commercial program SCIA ENGINEER and solved using the finite element method (FEM).

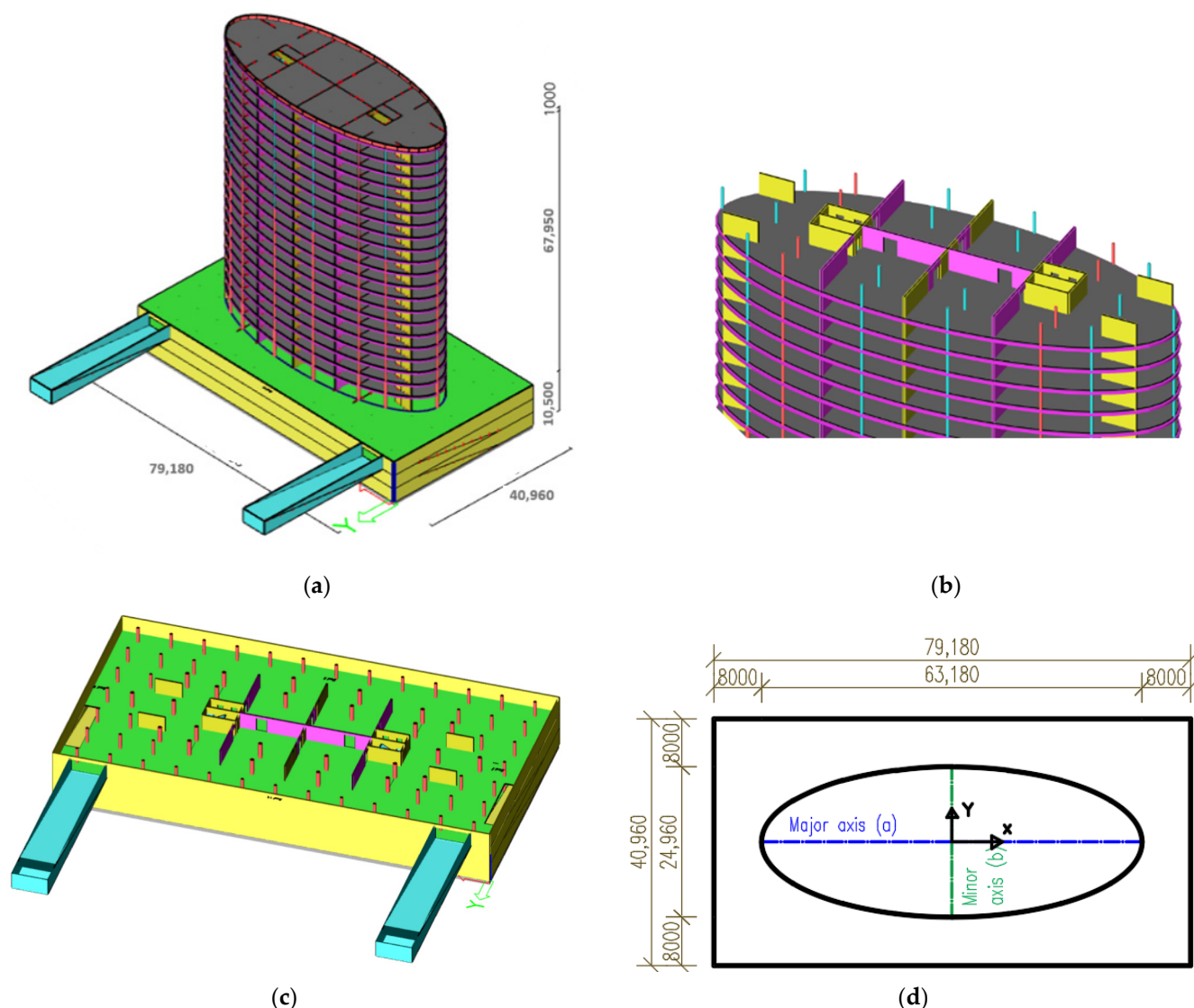


**Figure 2.** (a) Investigated building dimensions in mm; (b) typical floor; (c) underground part—parking spots; (d) the ground plan—dimensions in mm.

### 3. The Analysis of the Effects of Wind on the Elliptical Cylinder

When a real structure is designed or advising is given for a real structure, the appropriate values of external pressure coefficients, the values of wind velocities at considered heights, and the prevailing wind directions (from the roses of prevailing wind directions in a given area) should be used. External pressure coefficients should be taken from standards or from studies. In our case, external pressure coefficients for this kind of structure were not mentioned in the standards [20,21]. Therefore, three other methods were used for their determination. Firstly, a reduced-scale model of the building was tested in a wind tunnel. Then, these results were compared with the results of the CFD simulation. The last method was “the simplification of elliptic shape” and the use of the data from the standards [20,21].

#### 3.1. The Reduced-Scale Model and the Wind Tunnel

A reduced-scale model of the stand-alone structure in 1:390 scale was placed in the rear operating space of a boundary layer wind tunnel (BLWT) where turbulent wind flow is developed. Detailed information about the universal wind tunnel which belongs to Slovak University of Technology in Bratislava can be found in [22]. External wind pressures on the surface of the model were measured using the 16-channel pressure scanner SCANIVALVE DSA 3217/16Px with a maximum sampling frequency of 500 Hz for all

measuring points at the same time and with the accuracy of the results equal to  $\pm 0.05\%$ . The turbulence intensity and wind velocity profile were measured using a miniCTA 54T42 hot-wire anemometer (Dantec Dynamics). The development of both mentioned parameters is depicted in Figure 3.

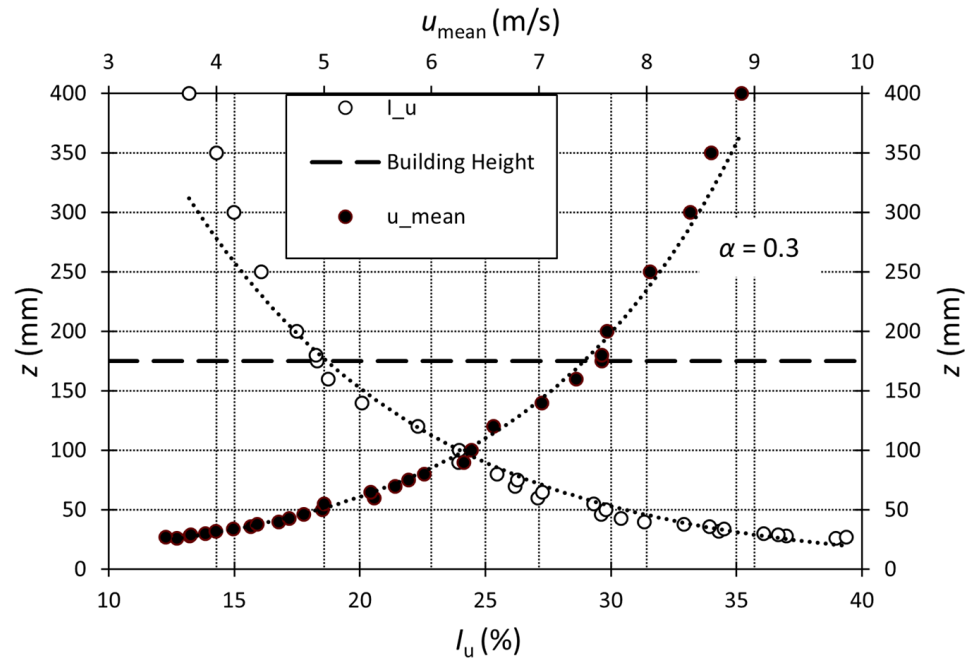


Figure 3. The turbulence intensity  $I_u$  (%) and mean wind velocity  $u_{mean}$  (m/s).

The reference wind velocity on the top of the model (measured without the model) was 13.76 m/s (barometric pressure was 101 140 Pa; air temperature was 19.40 °C). The model had two axes of symmetry. Therefore, the wind direction was applied only on one quadrant of the cross-section (see Figure 4), with the step of 10°. More information about the wind tunnel tests of an elliptical cylinder can be found in [23].

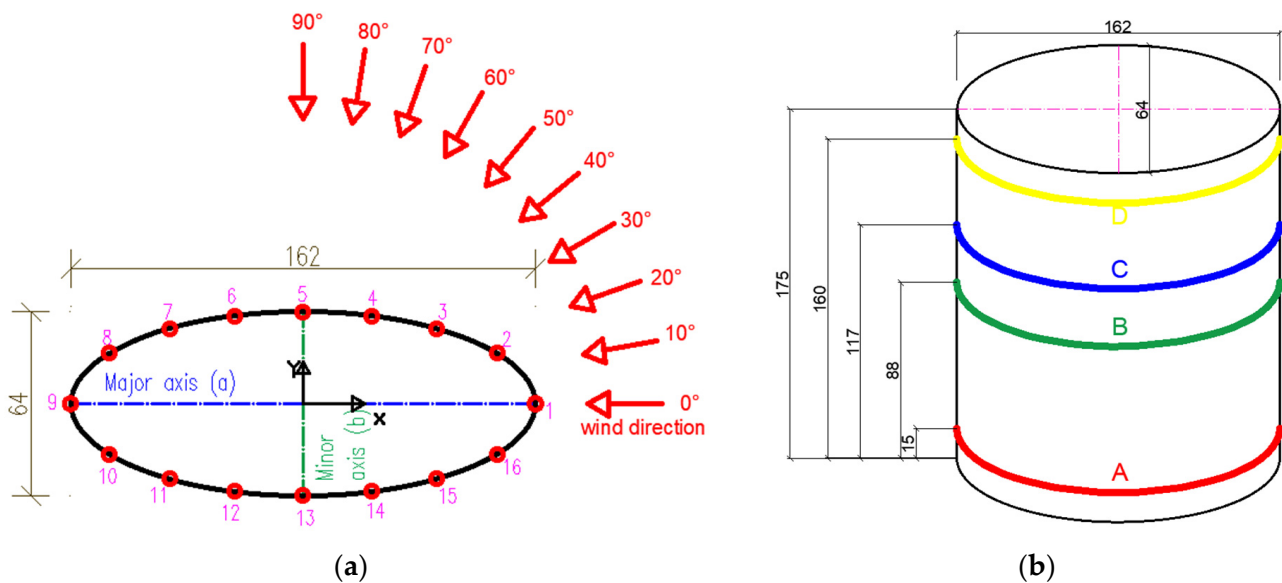
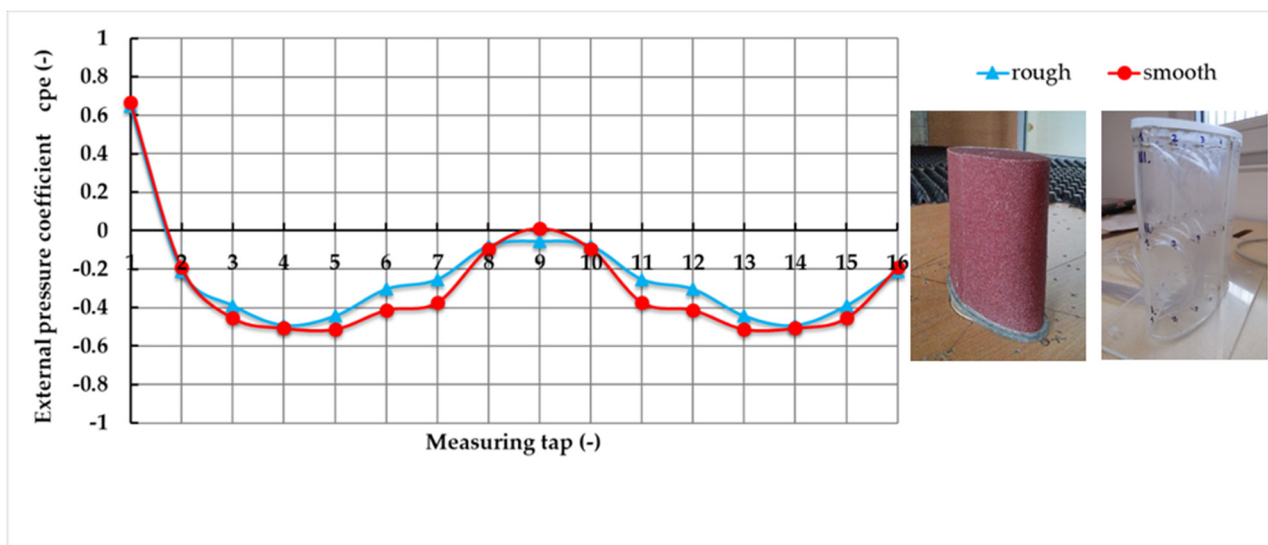


Figure 4. Reduced-scale model—dimensions are in mm: (a) measuring taps (1–16) and wind directions ( $0^\circ$ – $90^\circ$ ); (b) measured levels—A, B, C, D.

One of the many problems of testing in a wind tunnel is the meeting of the Reynolds number. If the calculated Reynolds number of the model is less than the recommended value for fully turbulent flow, the flow attacking the model is laminar or “transient”. For curved buildings, studies by various authors [24–26] declared that the minimal  $Re$  from  $1.4$  to  $6.5 \times 10 \times 10^5$  for fully turbulent flow should be larger than  $5 \times 10^5$  (for an angular building shape, larger than  $5 \times 10^4$ ). “Transient flow” is defined by a critical Reynolds number. Laminar flow is defined by the Reynolds number for laminar wind flow. All these Reynolds numbers can be determined by wind tunnel tests or CFD simulations. The  $Re$  of an experiment and CFD was from  $3.2 \times 10 \times 10^4$  to  $8.1 \times 10 \times 10^4$ , depending on the wind direction and thus the characteristic dimension of the model.

The reduced-scale model was made of plexiglass with a thickness of 5 mm. This material is heavier than the material used in 3D printing. So, the model was stiffer and also resistant to possible vibrations during the tests. The surface of the model was smooth. The dimensions were as follows: 64 mm—minor axis; 162 mm—major axis; 175 mm—the height. In total, 16 measuring taps were placed on the perimeter of the elliptical cylinder in all measured levels A–D (Figure 4).

In the case of a smooth surface, the Reynolds number was too small. The solution could be an increase in wind velocity, an increase in characterized length, or a change in the roughness of the surface. The third possibility was chosen, and the surface of the model was changed by the application of sandpaper with a roughness height of 0.8 mm. A comparison of external pressure coefficients is shown in Figure 5. The values of  $c_{pe}$  are lower for the modified model due to flow separation and applied roughness on the surface. More information about the Reynolds number of the model with the smooth/rough surface and the critical value of the Reynolds number can be found in [27].



**Figure 5.** The comparison of external pressure coefficients—rough surface vs. smooth surface.

External pressure coefficients  $c_{pe}$  were calculated by using the following expression:

$$c_{pe} = \frac{P_{WT}}{0.5 \times \rho \times v_{ref}^2} \quad (1)$$

where  $P_{WT}$  is the external wind pressure on the surface of the model measured in a wind tunnel (Pa) and  $v_{ref}$  is the reference wind velocity at the height of the top of the structure (m/s). The air density  $\rho$  ( $\text{kg}/\text{m}^3$ ) is a function of measured air temperature  $T$  in  $^\circ$  and barometric pressure BP in Pa.

$$\rho = \frac{BP}{(288.3 \times (T + 273.15))} \quad (2)$$

The comparisons of  $c_{pe}$  for all four levels and for three wind directions are presented in Figures 6–8.

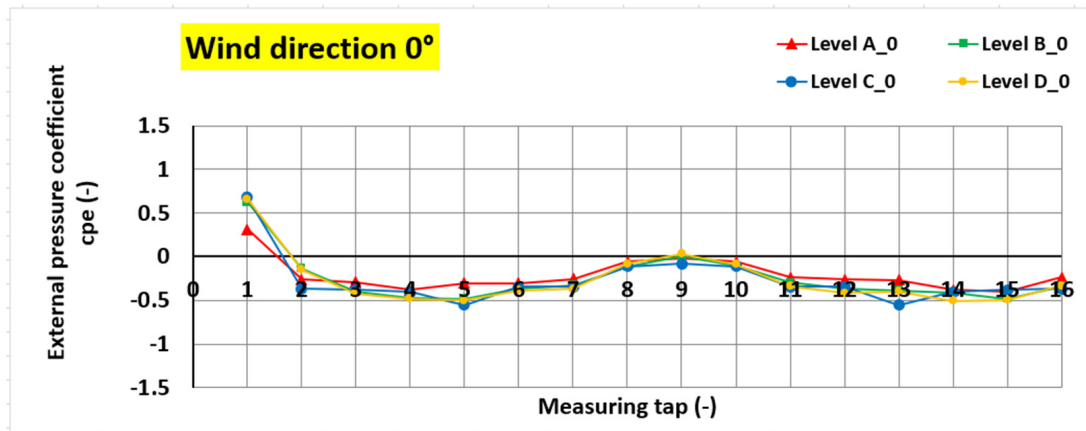


Figure 6. The comparison of  $c_{pe}$ —the levels A, B, C, D—wind direction 0°.

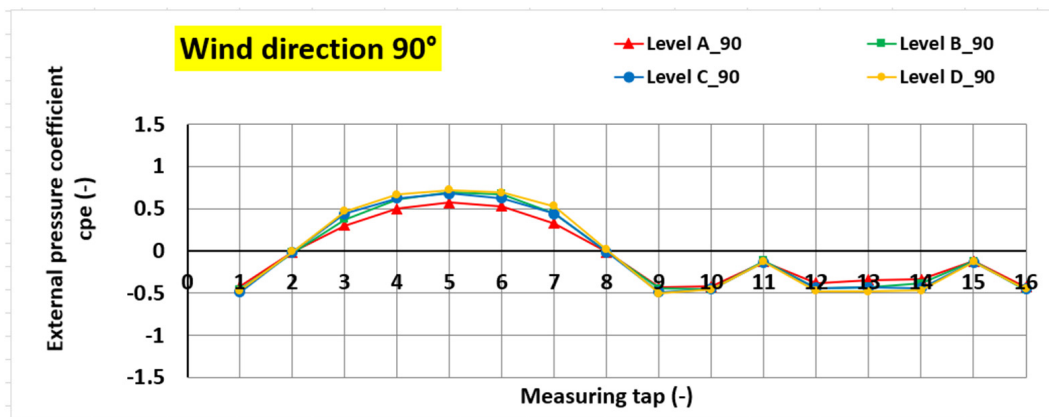


Figure 7. The comparison of  $c_{pe}$ —the levels A, B, C, D—wind direction 90°.

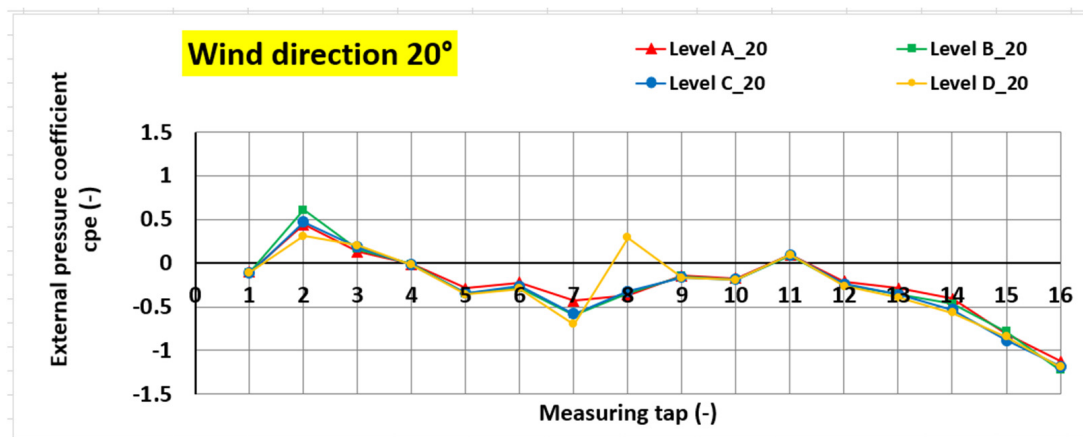


Figure 8. The comparison of  $c_{pe}$ —the levels A, B, C, D—wind direction 20°.

The calculated  $c_{pe}$  values were approximately the same for all levels. Therefore, simplification by using the “envelope of the data” was adopted, and maximum positive/negative pressures were considered in the further calculations. The values of  $c_{pe}$  are listed in Table 1.

**Table 1.** The comparison of  $c_{pe}$ —mean values vs. “the envelope of the data”.

Measuring Point (-)	Mean Values			“Envelope of the Data”		
	0°	90°	20°	0°	90°	20°
1	0.57	−0.46	−0.11	0.68	−0.49	−0.11
2	−0.23	−0.02	0.46	−0.37	−0.02	0.61
3	−0.37	0.40	0.17	−0.42	0.47	0.20
4	−0.43	0.60	−0.02	−0.48	0.67	−0.02
5	−0.46	0.67	−0.33	−0.55	0.72	−0.36
6	−0.35	0.63	−0.27	−0.39	0.69	−0.29
7	−0.32	0.43	−0.58	−0.37	0.53	−0.70
8	−0.09	−0.01	−0.18	−0.12	−0.02	−0.36
9	−0.02	−0.47	−0.16	−0.08	−0.51	−0.17
10	−0.09	−0.45	−0.19	−0.11	−0.46	−0.19
11	−0.30	−0.13	0.09	−0.35	−0.14	0.10
12	−0.35	−0.44	−0.24	−0.41	−0.48	−0.26
13	−0.40	−0.42	−0.35	−0.55	−0.48	−0.39
14	−0.42	−0.41	−0.49	−0.50	−0.47	−0.57
15	−0.44	−0.13	−0.83	−0.49	−0.14	−0.89
16	−0.32	−0.45	−1.18	−0.37	−0.47	−1.22

The values of  $c_{pe}$  were necessary for the estimation of the most unfavorable wind direction with respect to the shape of the structure. Firstly, the peak velocity pressures (Figure 9) were calculated for all four levels according to [20,21] by using Equations (3) and (4). Then, these values were used for the calculation of the external wind pressures using Equation (5). After that, the resultant forces  $R$  (kN) and torsional moments  $M_r$  (kNm) were determined for all considered wind directions. The maximum value of resultant force and maximum value of torsional moment gave the information on which wind direction is the most dangerous for the investigated structure.

$$q_p(z_e) = [1 + 7 \times I_v(z_e)] \times 0.5 \times \rho \times v_m^2(z_e), \quad (3)$$

$$v_m(z) = c_r(z) \times c_o(z) \times v_b, \quad (4)$$

$$w_e = q_p(z_e) \times C_{pe}. \quad (5)$$

where  $w_e$  is the external wind pressure (Pa),  $q_p(z_e)$  is the peak velocity pressure at the height  $z_e$  (m) in Pa,  $c_{pe}$  is the external pressure coefficient (-),  $I_v(z_e)$  is the turbulence intensity (-),  $\rho$  is the air density ( $\text{kg}/\text{m}^3$ ), and  $v_m(z_e)$  is the mean wind velocity at the height  $z_e$  (m/s). The turbulence intensity represents the fluctuation part of wind flow and is a function of turbulence factor  $k_1$ , orography factor  $c_o$ , and roughness length  $z_0$ .  $c_r(z)$  is the roughness factor, and  $v_b$  is the basic wind velocity (m/s) calculated by directional factor  $c_{dir}$  (-), seasonal factor  $c_{season}$  (-), and fundamental value of the basic wind velocity  $v_{b,0}$  (m/s). These parameters are defined in [20,21].

In this analysis, the terrain category between III and IV (close to IV) according to [21] was considered (the urban terrain, e.g., Bratislava). In the wind tunnel, it was modeled by the combination of FASTRADE 20 plastic film with a rectangular wooden barrier (with a height of 150 mm). This setting was verified by previous measurements of the vertical velocity profiles.

The resultant forces and maximum torsional moments are listed in Tables 2–5. The maximum resultant force was calculated for the wind direction of 90°, where the wind is applied on the large area of the structure. On the contrary, the wind direction of 0° had a minimal effect. The maximum torsional moments were calculated for the wind direction of

20°. The results matched well with the results of previously mentioned studies (Section 1). An example of the resultant forces and torsional moments is shown in Figure 10.

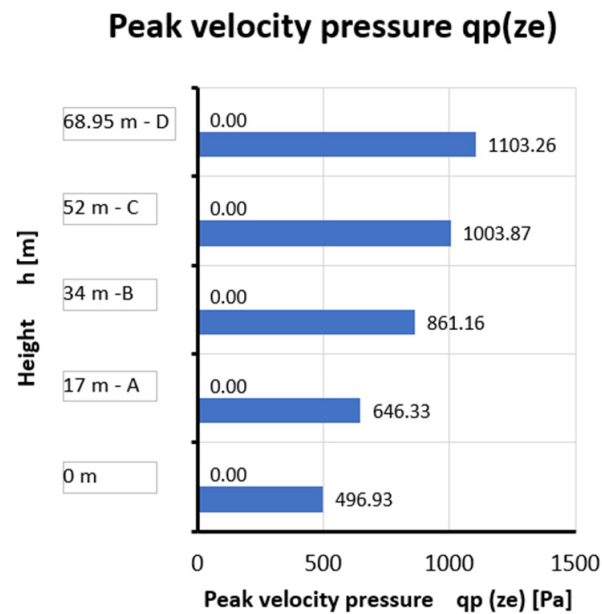


**Figure 9.** Peak velocity pressures calculated for measured levels.

**Table 2.** Resultant values—level A—5.85 m above the ground.

Wind Direction (°)	Resultant Force (kN)	Force Arm (m)	Angle of the Force (°)	Torsional Moment (kNm)
0	0.34	−77.48	147	−26.48
20	27.55	−29.74	275	−819.35
90	60.95	0.44	270	26.94

**Table 3.** Resultant values—level B—34.32 m above the ground.

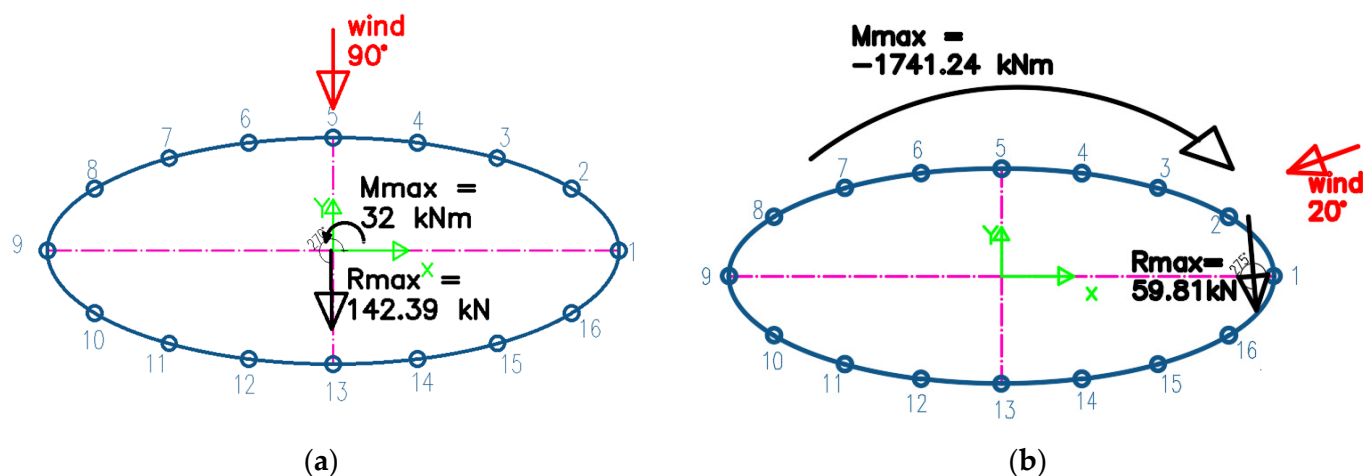
Wind Direction (°)	Resultant Force (kN)	Force Arm (m)	Angle of the Force (°)	Torsional Moment (kNm)
0	8.65	−15.00	188	−129.77
20	51.76	−31.02	272	−1605.58
90	126.42	0.61	271	77.20

**Table 4.** Resultant values—level C—45.63 m above the ground.

Wind Direction (°)	Resultant Force (kN)	Force Arm (m)	Angle of the Force (°)	Torsional Moment (kNm)
0	10.99	−0.04	180	0.47
10	30.47	−33.43	265	−1018.50
20	59.81	−29.11	275	−1741.24
30	71.47	−22.85	270	−1632.84
40	83.78	−17.42	266	−1459.28
50	104.23	−12.69	264	−1322.31
60	124.84	−9.16	265	−1143.94
70	133.43	−6.46	266	−862.02
80	149.04	−3.35	268	−499.85
90	142.39	0.22	270	32.00

**Table 5.** Resultant values—level D—62.40 m above the ground.

Wind Direction (°)	Resultant Force (kN)	Force Arm (m)	Angle of the Force (°)	Torsional Moment (kNm)
0	11.05	−13.25	202	−146.36
20	77.43	−19.64	281	−1520.86
90	171.19	0.52	270	88.96

**Figure 10.** Resultant forces  $R_{\max}$  and torsional moments  $M_{\max}$ —level C: (a) wind 90°; (b) 20°.

### 3.2. CFD Simulation in the Program ANSYS FLUENT

The aim of this paper is not to provide comprehensive information about the CFD simulation and obtained results. Only basic information is mentioned. A CFD simulation was created and solved using the commercial program ANSYS FLUENT. For the solution, two well-known Reynolds-averaged Navier–Stokes equation turbulence models were used: the realizable  $k$ - $\epsilon$  model and the shear-stress transport (SST)  $k$ - $\omega$  model. Steady simulations were run. The reference wind velocity on the top of the structure, the vertical velocity profile, and the turbulence intensity profile from wind tunnel tests were used.

The model was created in the scale of 1:390. The size of the computational domain was  $2.6 \times 1.6 \times 3$  m ( $W \times H \times L$ ). Two different types of mesh elements were used—cut-cell elements and tetrahedron elements. Simulations were calculated in three dimensions, and the ground was simulated with the sand grain roughness. It represented the terrain category between III and IV (close to IV) according to the wind standard [21]. Detailed information about the CFD simulation, including the descriptions of selected turbulence models, the considered input parameters, the settings and boundary conditions, the meshing, and the obtained results, can be found in [27]. A good coincidence between the values from CFD and from wind tunnel tests was achieved (Figure 11). The verified CFD simulation was used for further analyses, e.g., determination of the pressure distribution on the roof. A grid sensitivity report was performed, and the results are illustrated in Figure 12. The mesh and streamlines are presented in Figure 13.

The  $c_{pe}$  values calculated for three roof alternatives—a totally flat roof, a roof with a roof parapet of 500 mm, and a roof with a roof parapet of 2500 mm—are compared in Figure 14. The last alternative should be used for the design of modern green fully useful roofs (sport and relaxation zones with vegetation).

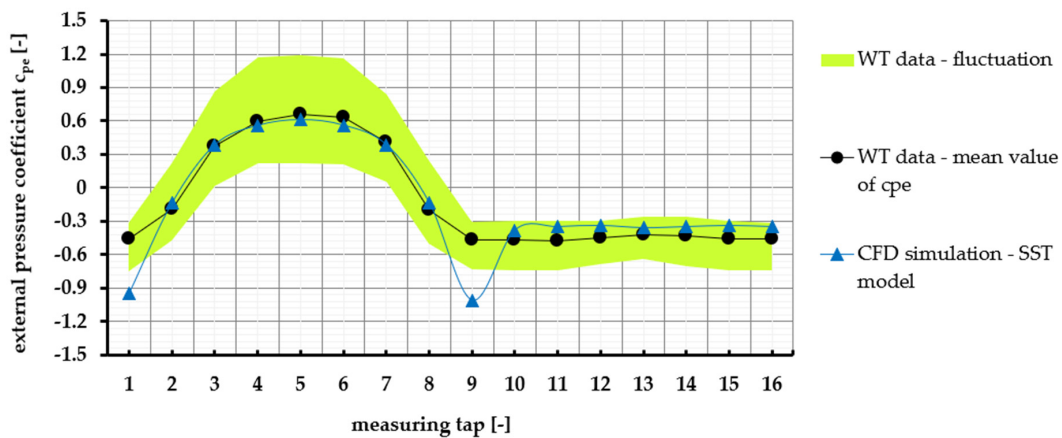


Figure 11. The values of  $c_{pe}$  obtained for wind direction  $90^\circ$ —WT tests vs. CFD.

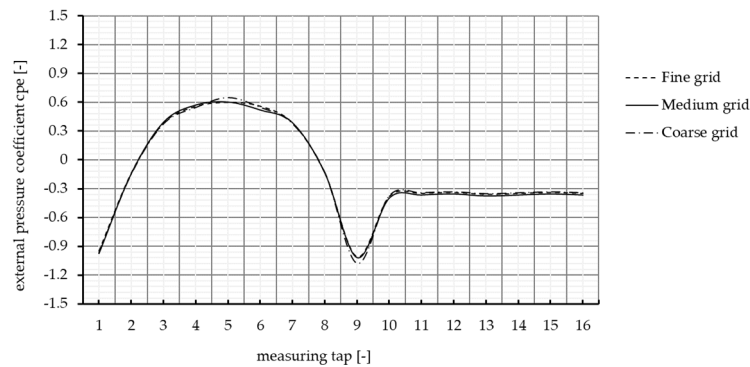


Figure 12. The grid sensitivity test.

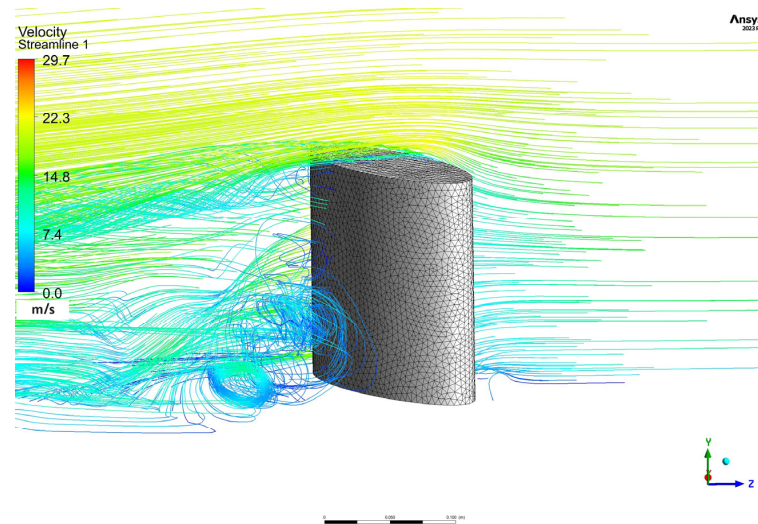
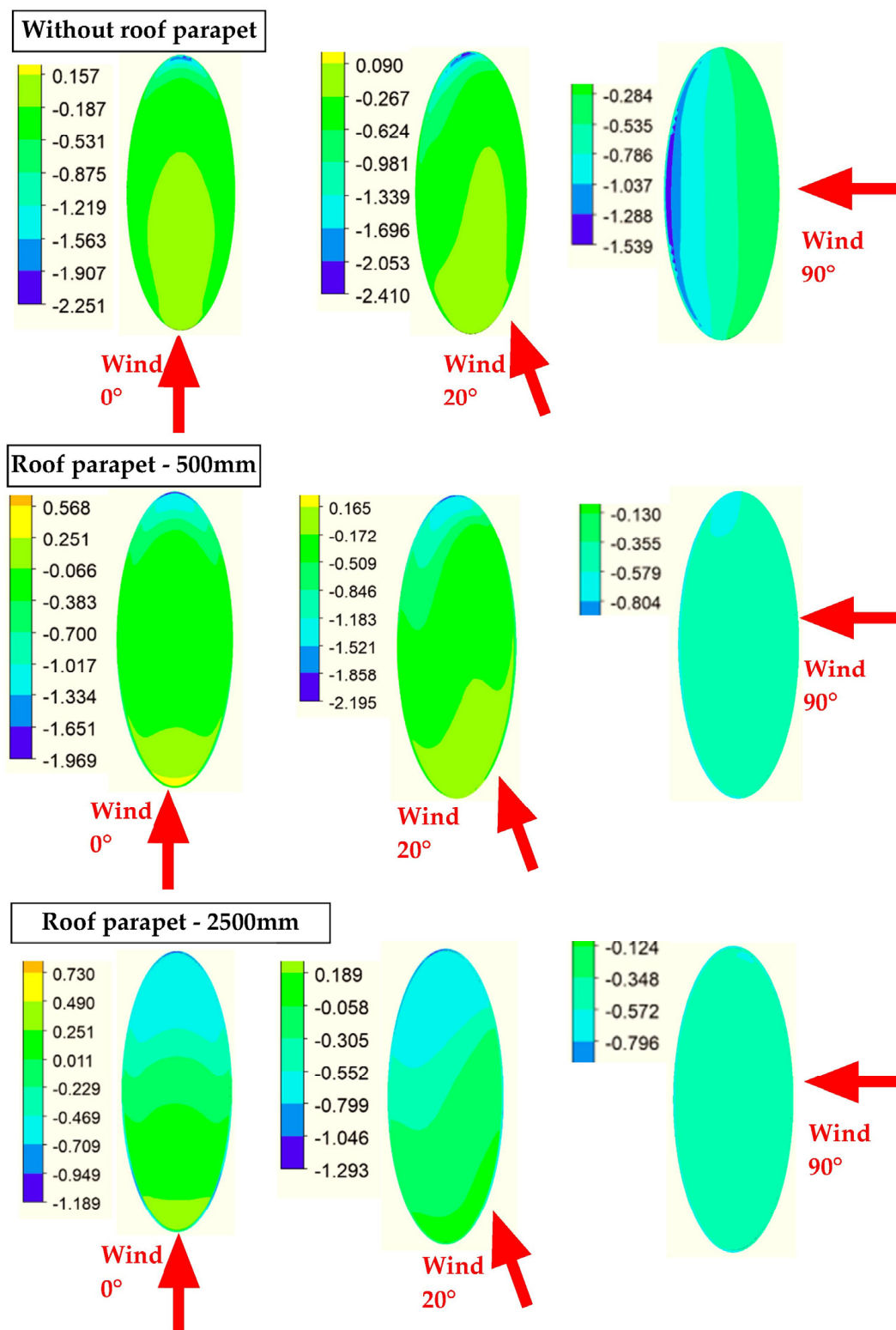


Figure 13. Mesh grid and streamlines for wind direction  $45^\circ$ . There were no measuring taps on the roof of test model. Therefore, CFD simulation was a useful tool for the determination of  $c_{pe}$ . The roof of the model was totally flat (Figure 5). In the case of a real structure, it should be enclosed by a roof parapet. In static and dynamic analysis, a roof parapet with a height of 1 m was considered. The model created for the CFD had a roof parapet with a height of 0.5 m. The explanation is as follows: In the model used for static and dynamic analysis, the layers of the roof are considered only as the area load. But in the case of CFD analysis, the model is created as “an envelope of the structure”.



**Figure 14.** The values of  $c_{pe}$  calculated by CFD for three alternatives of the roof.

### 3.3. The Simplification of the Elliptic Shape

The wind tunnel tests provide the best results, but this method is expensive and time-consuming. On the other hand, the CFD simulation seems to be a faster method, but there are many problems. It was confirmed by many studies that the selection of the turbulence model, consideration of the appropriate input parameters, and setting of the simulation are

crucial. Without the verification by the wind tunnel test, the solution provided by a CFD simulation is only a “prediction”, and there is a relatively large risk regarding whether the results are correct. Regarding the above-mentioned facts, we tried to “simplify” the shape of the ground plan and used the information defined in the standards [20,21].

In the first case, the ellipse was divided into two small semi-circles and one rectangle (Figures 15 and 16).

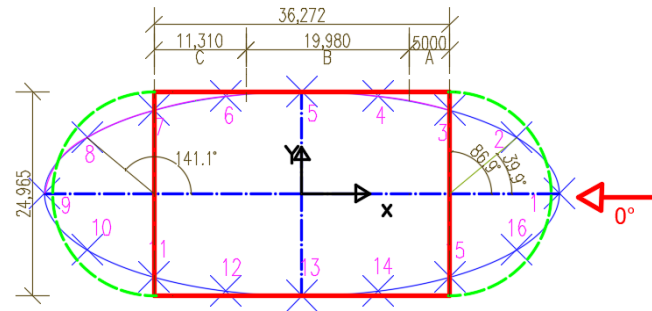


**Figure 15.** Alternative No. 1—wind direction 0°.

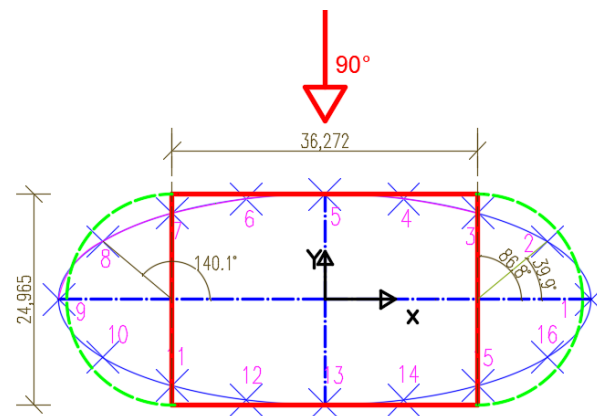


**Figure 16.** Alternative No. 1—wind direction 90°.

The pressure coefficients on the semi-circles were calculated by using the Reynolds number  $R_e$ , defined as follows:

$$R_e = \frac{b \times v(z_e)}{\nu} \quad (6)$$

$$v(z_e) = \sqrt{\frac{2 \times q_p(z_e)}{\rho}} \quad (7)$$

where  $b$  is the diameter (m),  $\nu$  is the kinematic viscosity of the air ( $1.5 \times 10^{-7} \text{ m}^2/\text{s}$ ),  $v(z_e)$  is the peak wind velocity (m/s) at height  $z_e$  (m),  $q_p(z_e)$  is the peak wind pressure (Pa) calculated by using Equation (3), and  $\rho$  is the air density ( $1.25 \text{ kg/m}^3$ ). In our case,  $b = 24.965 \text{ m}$ ,  $q_p(z_e) = 1103.26 \text{ Pa}$ ,  $v(z_e) = 42.01 \text{ m/s}$ . The resultant Reynolds number was  $6.99 \times 10^7$ .

The external pressure coefficients were calculated according to [20,21]:

$$c_{pe} = c_{p,0} \times \psi_{\lambda\alpha} \quad (8)$$

where  $c_{p,0}$  is the external pressure coefficient without free-end flow depending on Reynolds number (depicted in Graph 7.27 in [20]).  $\psi_{\lambda\alpha}$  is the end-effect factor defined as follows:

$$\psi_{\lambda\alpha} = 1 \quad \text{for } 0^\circ \leq \alpha \leq \alpha_{min} \quad (9)$$

$$\psi_{\lambda\alpha} = \psi_{\lambda} + (1 - \psi_{\lambda}) \times \cos\left(\frac{\pi}{2} * \left(\frac{\alpha - \alpha_{min}}{\alpha_A - \alpha_{min}}\right)\right) \quad \text{for } \alpha_{min} \leq \alpha \leq \alpha_A \quad (10)$$

$$\psi_{\lambda\alpha} = \psi_{\lambda} \quad \text{for } \alpha_A \leq \alpha \leq 180^{\circ} \quad (11)$$

where  $\alpha_A$  is the position of the flow separation ( $^{\circ}$ ),  $\alpha_{min}$  is the position of the minimum pressure ( $^{\circ}$ ), and  $\psi_{\lambda}$  is the end-effect factor (determined from Graph 7.36 in [20]). Two parameters had to be calculated: the solidity ratio  $\varphi$  and the slenderness  $\lambda$ . The solidity ratio was calculated using the following equation:

$$\varphi = A / A_c \quad (12)$$

where  $A$  is the sum of the projected areas of the members ( $m^2$ ) and  $A_c$  is the overall envelope area ( $m^2$ ).

Effective slenderness  $\lambda$  was determined for the case  $H \geq 50$  m as the minimum value from  $(0.7 \times H/b; 70)$ , according to the recommendation in [16]. A comparison of the results is shown in Figures 17 and 18.

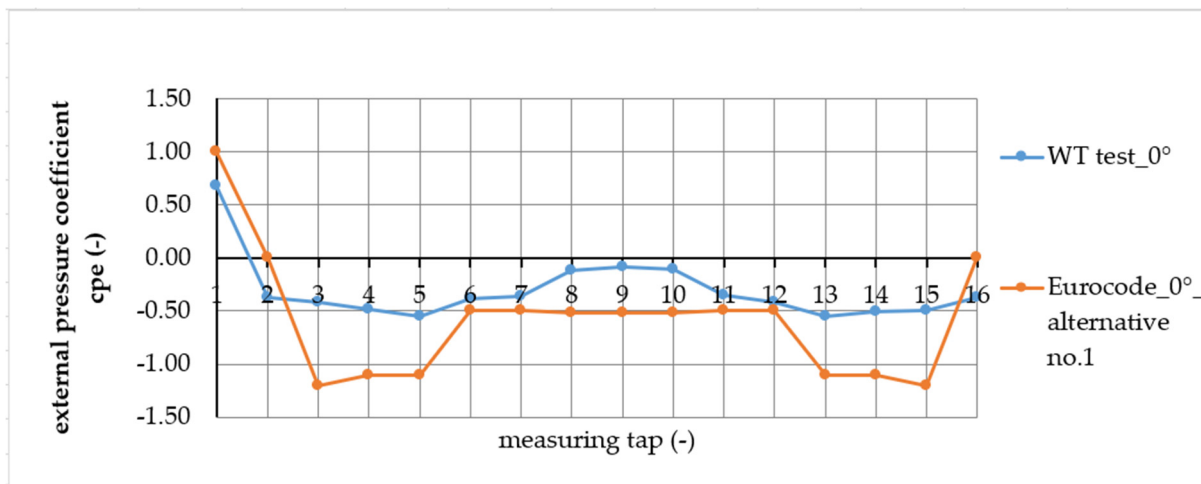


Figure 17. The results—alternative No. 1—wind direction  $0^{\circ}$ .

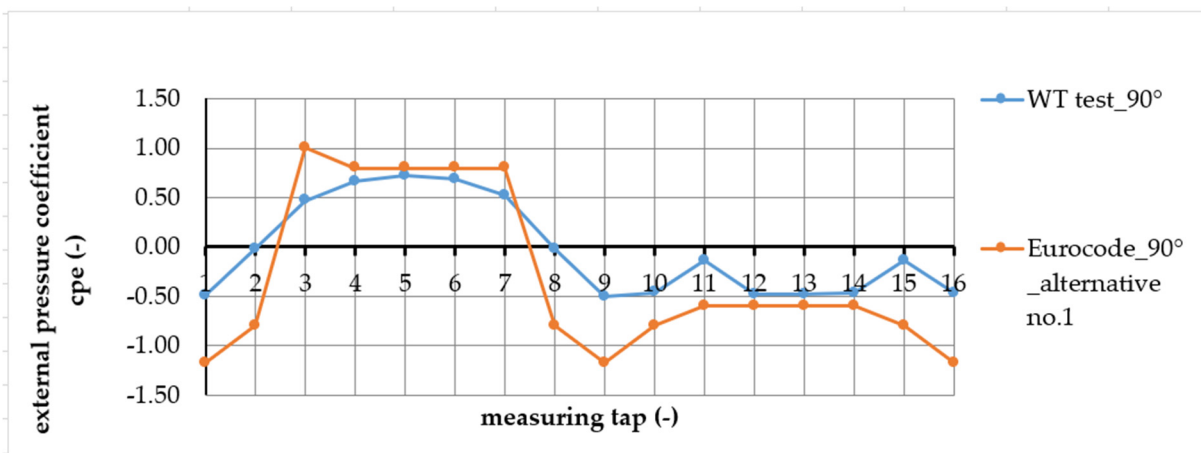


Figure 18. The results—alternative No. 1—wind direction  $90^{\circ}$ .

In the second case, the ellipse was compared with one big circle and one big rectangle (Figures 19 and 20). A New Reynolds number for the larger diameter of the circle was

calculated. In this case,  $b = 31.59$  m,  $q_p(z_e) = 1103.26$  Pa,  $v(z_e) = 42.01$  m/s. The resultant Reynolds number was  $8.85 \times 10^7$ . Also, the effective slenderness  $\lambda$  was recalculated.

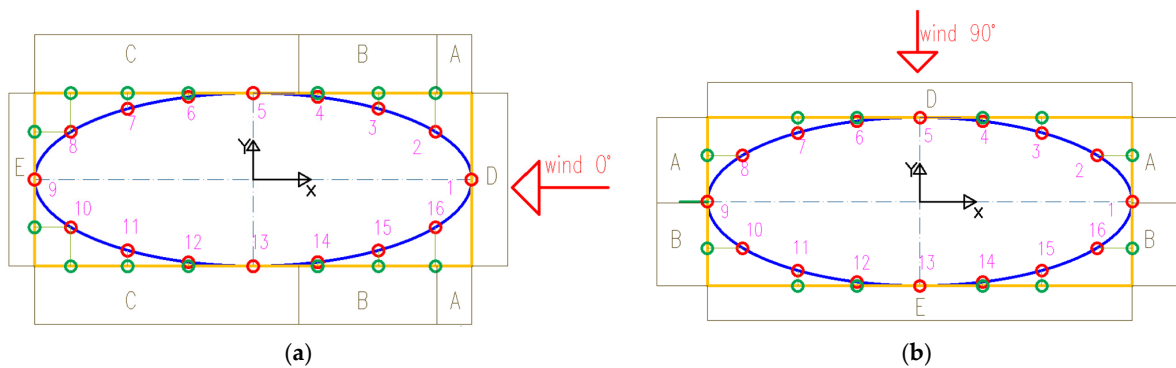


Figure 19. Alternative No. 2 (the comparison with the rectangle)—(a) wind direction  $0^\circ$ ; (b) wind direction  $90^\circ$ .

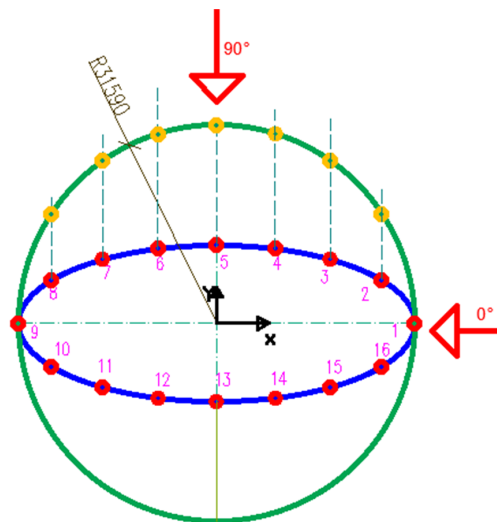


Figure 20. Alternative No. 2 (the comparison with the circle)—wind direction  $0^\circ$  and  $90^\circ$ .

The ellipse, rectangle, and circle are compared in Figures 21 and 22. The values of  $c_{pe}$  determined for the ellipse were significantly lower. It can be said that more realistic results are provided by the wind tunnel tests or the CFD simulation verified by tests.

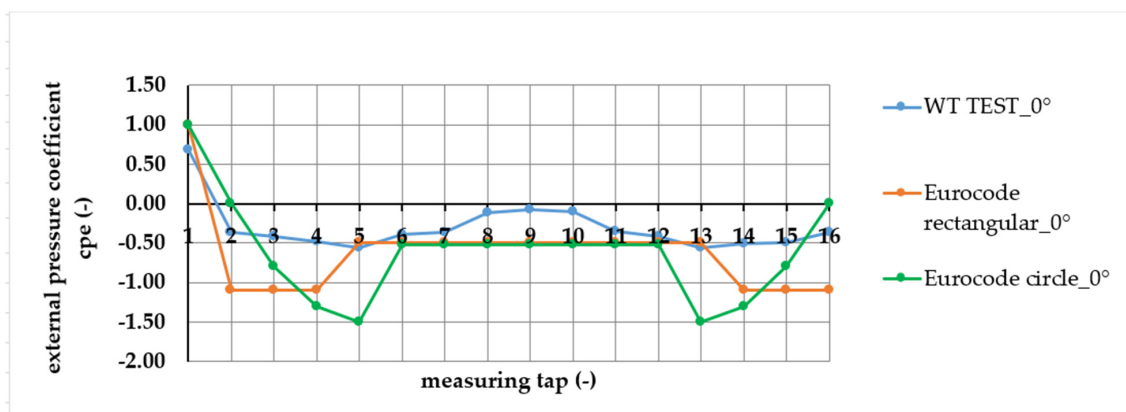


Figure 21. The results—alternative No. 2—wind direction  $0^\circ$ .

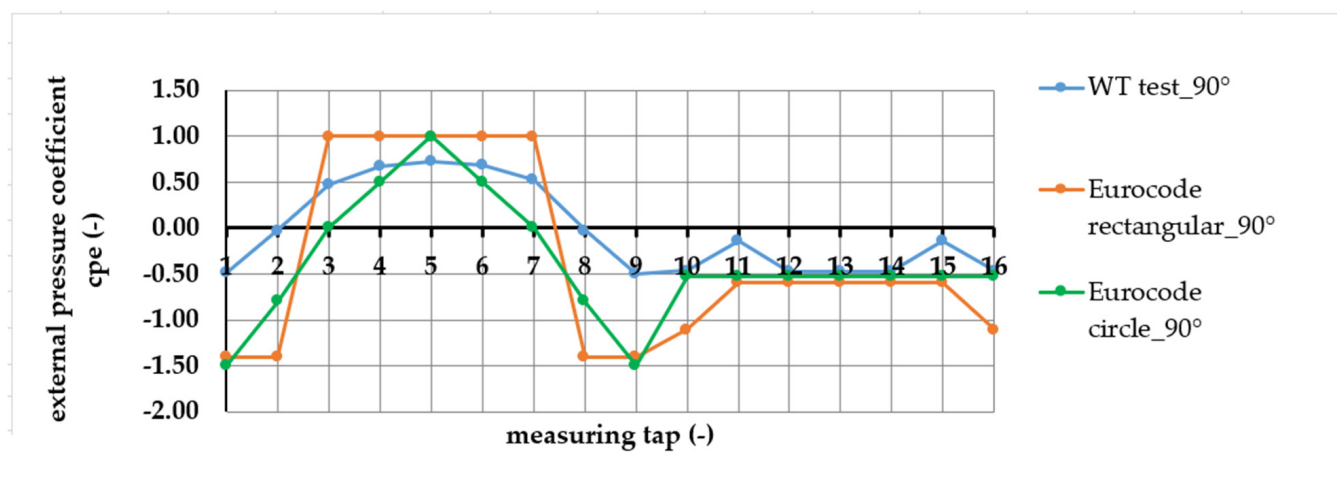


Figure 22. The results—alternative No. 2—wind direction 90°.

### 3.4. The Application of the Results to the 3D Model of the Building Used for Static and Dynamic Analysis

“The simplification of the shape” did not provide results with sufficient accuracy. Therefore, the values obtained from wind tunnel tests and the verified CFD simulation were used for the creation of a 3D model in the commercial program SCIA ENGINEER. The values of  $c_{pe}$  in all four levels determined for a particular wind direction were the same (the differences were very small). So, the external pressure coefficients were considered with the same values for all levels (Table 1—“Envelope of the data”). Wind load (kN) was applied on the surface of the structure in a horizontal direction—perpendicularly to the tangent line at a considered point. It was calculated by using the peak wind pressures at the considered height multiplied by the load width and load height at a given point. In our case, the load panels as a special element in the SCIA ENGINEER were not used because of computing capacity. Wind load was applied as a force load at 16 points on the perimeter of the ground plan in the places of all horizontal slabs. The following wind directions were considered for static analysis: 0° (it is parallel with the  $x$ -axis), 20° (it caused the maximum torsional moment), and 90° (it caused the maximum resultant force and is parallel with the  $y$ -axis).

## 4. Static Analysis

The design of a building can be divided into two analyses. The first is static analysis where the wind and snow loads have to be considered. The second type is dynamic analysis, without the wind and snow loads. The dynamic effect of an earthquake event is too fast, and the building does not have time to respond to the wind load. Snow load is not applied on the structure, because it is shaken fast. The whole building and all its elements have to satisfy the conditions defined for both the serviceability limit state (SLS) and the ultimate limit state (ULS).

### 4.1. Applied Loads

In the static analysis, the following loads were considered: The self-weight of all structural elements was calculated by the program automatically. The cladding and the weight of floor layers (varied values calculated according to the utilization of the floors) were considered as permanent loads. The characteristic values of the weight of floor layers were 2.79 kN/m<sup>2</sup> (underground floors), 1.66 kN/m<sup>2</sup> (commercial spaces, technical floor, and the flats), 0.69–1.25 kN/m<sup>2</sup> (the stairs), and 3.85 kN/m<sup>2</sup> (the roof). The characteristic values of variable loads were considered according to the utilization of the floors [28,29]: 2.5 kN/m<sup>2</sup> (underground floors), 3 kN/m<sup>2</sup> (commercial spaces), 2 kN/m<sup>2</sup> (the flats), 3 kN/m<sup>2</sup> (the stairs), 4 kN/m<sup>2</sup> (technical floor), 0.75 kN/m<sup>2</sup> (the roof). Partition walls were

considered as variable loads (with a characteristic value equal to  $1.2 \text{ kN/m}^2$ ). The wind load was taken from the previous analysis (see Section 3.4). The snow load was calculated according to [30,31]. The resultant characteristic value of snow load on the ground was equal to  $0.48 \text{ kN/m}^2$  (altitude of the site 138 m, zone III in the snow map of Slovakia, roof snow load shape coefficient 1.0, thermal coefficient 1.0, flat roof). Advising was given for the most unfavorable combination of applied loads for the building.

#### 4.2. The Subsoil Stiffness Coefficient

The soil category B according to [19] was considered under the structure (the layers of mediumly compressed sands, gravels, or mediumly rigid clays with shear wave velocity in the range of 360–800 m/s). Soil–structure interaction was considered using Winkler’s two-parameter model [32]. The subsoil stiffness coefficient  $k$  ( $\text{kN/m}^3$ ) was calculated as follows:

$$k = p/s. \quad (13)$$

where  $p$  is the foundation reaction calculated from characteristic values of applied loads ( $\text{kN/m}^2$ ) and  $s$  is soil displacement calculated from the soil parameters ascertained by a hydrogeological survey or from the literature (m).

The subsoil stiffness coefficient was taken with full value in the vertical direction. In the horizontal direction, only 50% of its value was considered. According to the recommendations defined in [32], the value of the subsoil stiffness coefficient for compressed gravel in the vertical direction is in the range of 60–100  $\text{MN/m}^3$ .

The groundwater level was considered at the height of the foundation plate; therefore, the bulk density of the soil  $\rho$  and correction coefficient  $m$  were lower (with the influence of water). Soil parameters were taken from [33] (G2-GP, Id (0.33–0.67),  $\rho = 10.8 \text{ kN/m}^3$ ,  $m = 0.2$ ,  $E_{\text{def}} = 50,000 \text{ kPa}$ , Poisson’s ratio  $\nu = 0.2$ , conversion coefficient between the values of  $E_{\text{def}}$  and  $E_{\text{oed}}$  is  $\beta = 0.9$ ). The resultant value of the soil displacement calculated using Equation (14) was 5.2 mm. It was lower than the limit value defined for multi-story buildings with wall structural systems made of monolithic reinforced concrete  $w_{\text{lim}} = 60 \text{ mm}$  [33]. The calculated subsoil stiffness coefficient was  $40,420 \text{ kN/m}^3$ .

$$s = \sum_{i=1}^n \frac{\sigma_{zi} - m_i \times \sigma_{ri}}{E_{\text{oedi}}} \times h_i. \quad (14)$$

where  $\sigma_{zi}$  is the vertical component of increment stress ( $\text{kN/m}^2$ ) in the middle of the layer with the thickness of  $h_i$  (m),  $m_i$  is the correction coefficient (-),  $\sigma_{ri}$  is the vertical component of the original geostatic stress ( $\text{kN/m}^2$ ) in the middle of the layer,  $E_{\text{oedi}}$  is the oedometric modulus of deformation (kPa) calculated as  $E_{\text{def}}/\beta$  ( $E_{\text{def}}$  is the deformation modulus (kPa) and  $\beta$  is the conversion coefficient), and  $\nu$  is Poisson’s ratio (-).

$$\beta = 1 - \frac{2 \times \nu^2}{1 - \nu}. \quad (15)$$

The bearing capacity of soil is important for the stability analysis of the foundation. If the bearing capacity of soil is not sufficient, the following negative effects can occur: the soil displacement of the structure being too large, the inclination of the structure, the non-uniform settlement of the structure, and damage to the structure. The following requirement has to be satisfied:

$$\sigma_{de} \leq R_d. \quad (16)$$

where  $\sigma_{de}$  is extreme design contact stress on the bottom side of the foundation plate (kPa) with the consideration of short-term loads and  $R_d$  is the design bearing capacity of foundation soil (kPa).

$$R_d = c_d N_{cd} s_c d_c i_c g_c + \gamma_1 d N_{dd} s_d d_d i_d g_d + \gamma_2 \frac{b_{eff}}{2} N_{bd} s_b d_b i_b g_b. \quad (17)$$

where  $c_d$  is the design value of cohesion of soil (kPa).  $\gamma_1$  and  $\gamma_2$  are the bulk density of soil above/under the foundation ( $\text{kN}/\text{m}^3$ ).  $b_{eff}$  is the effective width of the foundation (m).  $N_{cd}$ ,  $N_{dd}$ , and  $N_{bd}$  are design bearing parameters depending on the design value of the angle of internal friction  $\varphi_d$  ( $^\circ$ ).  $s_c$ ,  $s_d$ , and  $s_b$  are parameters depending on the shape of the foundation (-).  $d_c$ ,  $d_d$ , and  $d_b$  are parameters depending on the depth of the foundation.  $i_c$ ,  $i_d$ , and  $i_b$  are parameters expressing the slope of applied loads. The parameters  $g_c$ ,  $g_d$ , and  $g_b$  express the slope of the building site. Effective values of soil parameters were considered. More information can be found in [33–35]. The resultant value of  $R_d$  was  $7660 \text{ kN}/\text{m}^2$ , and  $\sigma_{de} = 290 \text{ kPa}$ .

#### 4.3. The Limit Values

The maximum horizontal displacement  $u_{max}$  without the inclination of the footing bottom is defined as follows:

$$u_{cal} \leq u_{max} = H/2000 \quad (18)$$

where  $u_{cal}$  is the calculated horizontal displacement of the top story in the x-direction or y-direction and H is the height of the horizontal slab of the top story measured from the footing bottom. In this case, H was 80.25 m and  $u_{max}$  was 40 mm.

If this condition is not satisfied, the non-structural elements can be damaged (e.g., cracks on the internal and external surfaces of the walls, defects in plaster and wall tiling). This problem can be solved by adding other stiffening walls or by increasing the dimensions of the existing stiffening walls. Large horizontal displacements (or large vibrations) can have negative effects on the utilization of the building (e.g., the installation of sensitive broadcast devices on the top technical floor). Large vibrations of the building can also be dangerous for the people inside, having negative effects on their mental health [36].

The maximum vertical deflection  $v_{max}$  of a reinforced concrete horizontal slab was considered as  $L_{max}/250$ , where  $L_{max}$  is the maximum span. In our case,  $L_{max}$  was 6 m, and  $v_{max} = 24 \text{ mm}$ .

The model was solved using the finite element method (FEM). The size of 1D elements was 100 mm, and that of 2D elements was 400 mm. In total, 9040 1D elements and 395,375 2D elements were generated. For the calculation of vertical deflection, the maximum size of 2D elements was set as 100 mm.

## 5. Results

In the case of static analysis, the following assessments have to be performed: the assessment of maximum horizontal displacement at the top of the structure, the assessment of horizontal displacements between each pair of horizontal slabs, and the assessment of vertical deflection with the influence of a staggered arrangement of variable load. The design of all structural elements is based on the recommendations defined for the serviceability limit state and utilization limit state according to valid standards.

The calculated horizontal displacements for the combination of applied loads for the serviceability limit state, the subsoil stiffness coefficient  $k_z$  equal to  $50 \text{ MN}/\text{m}^3$ , and the wind directions of  $0^\circ$ ,  $20^\circ$ , and  $90^\circ$  are depicted in Figures 23–25.

The vertical deflection of the horizontal slab was calculated with the consideration of a staggered arrangement of variable load. The resultant values are depicted in Figures 26 and 27. The calculated 3D displacements are shown in Figures 28–30.

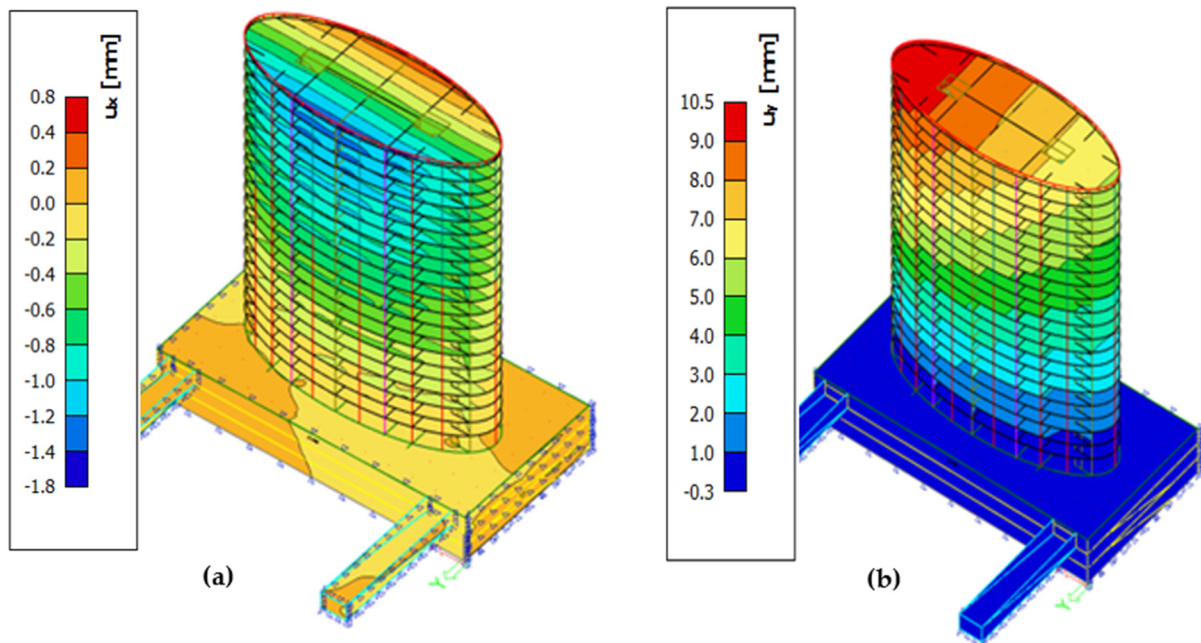


Figure 23. Wind direction 90°—(a) x-direction; (b) y-direction.

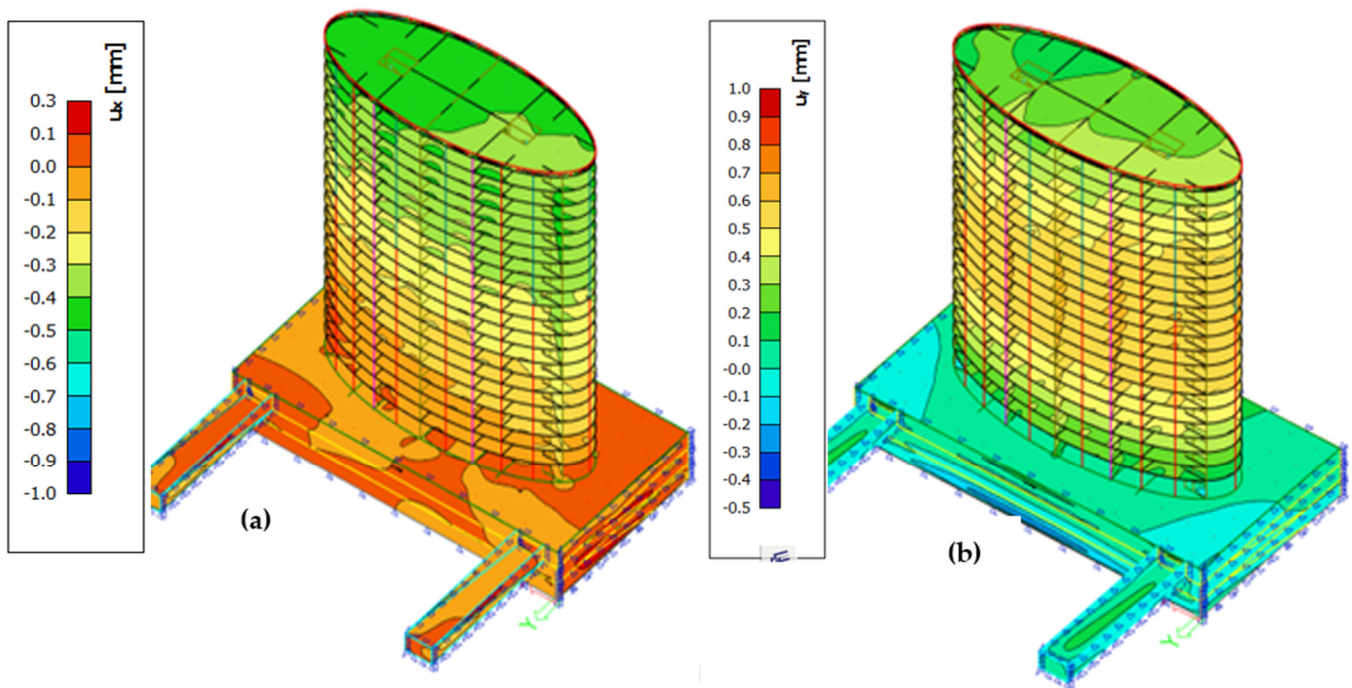


Figure 24. Wind direction 0°—(a) x-direction; (b) y-direction.

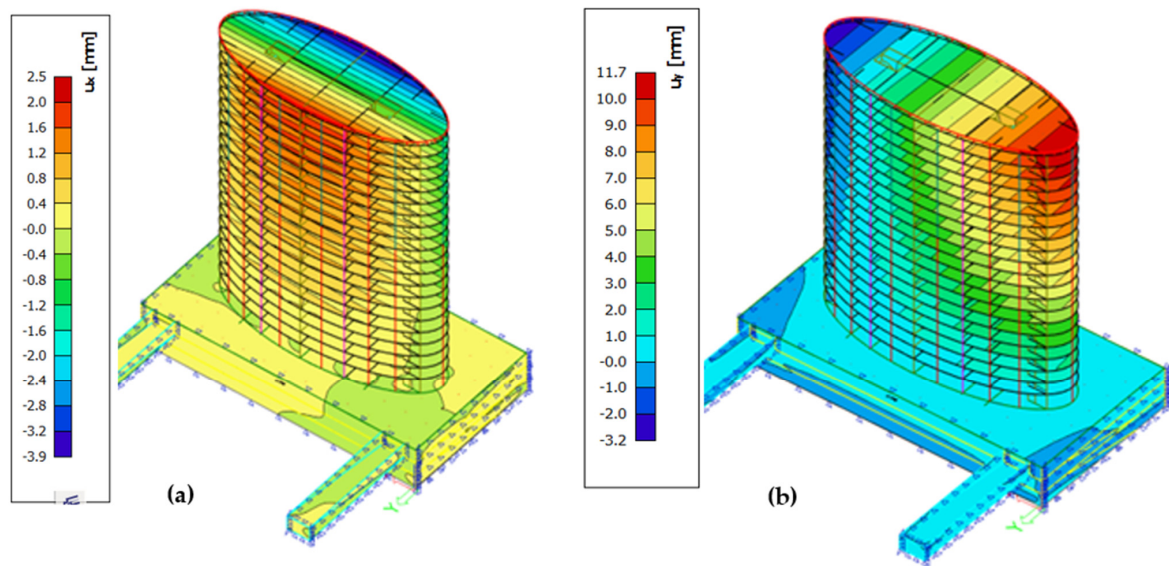


Figure 25. Wind direction 20°—(a)  $x$ -direction; (b)  $y$ -direction.

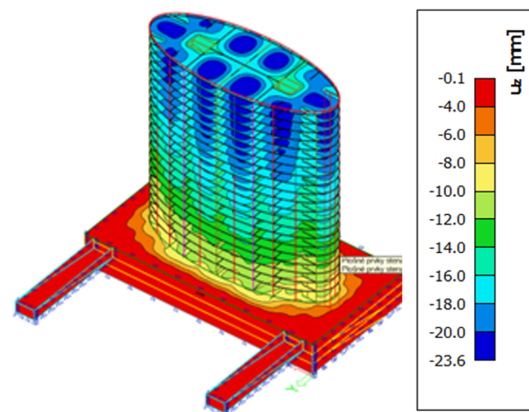


Figure 26. Vertical deflection calculated for  $k_z = 50,000 \text{ kN/m}^3$ , wind direction 20°.

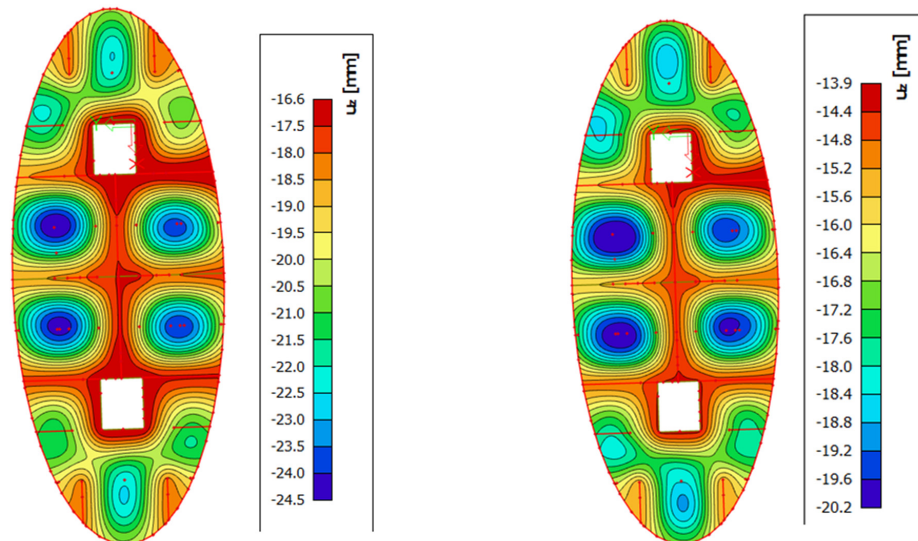


Figure 27. Vertical deflection calculated for  $k_z = 40,421 \text{ kN/m}^3$ , wind direction 20°.

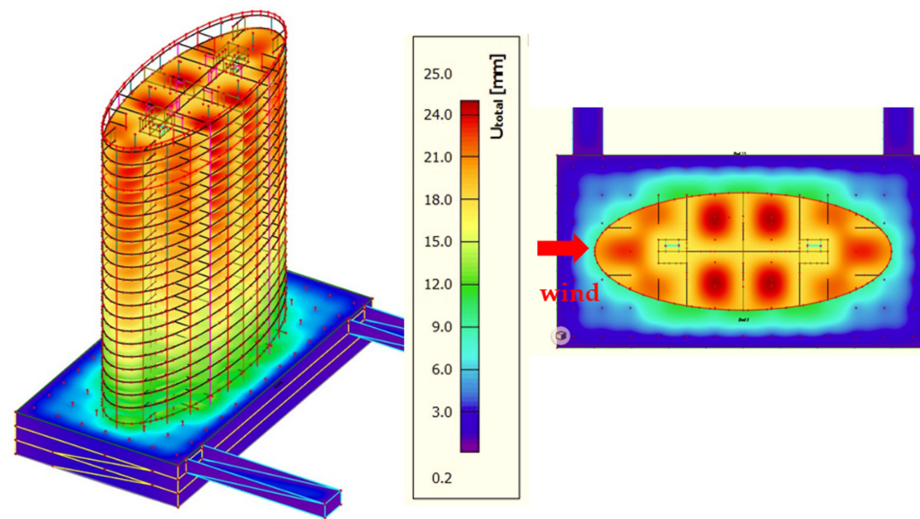


Figure 28. Three-dimensional deformation  $u_{tot}$  calculated for  $k_z = 40,421 \text{ kN/m}^3$ , wind direction  $0^\circ$ .

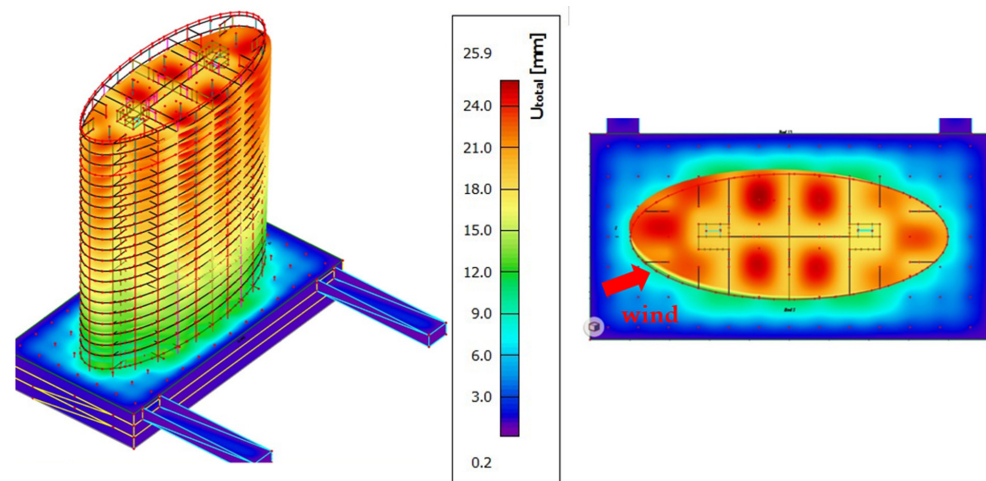


Figure 29. Three-dimensional deformation  $u_{tot}$  calculated for  $k_z = 40,421 \text{ kN/m}^3$ , wind direction  $20^\circ$ .

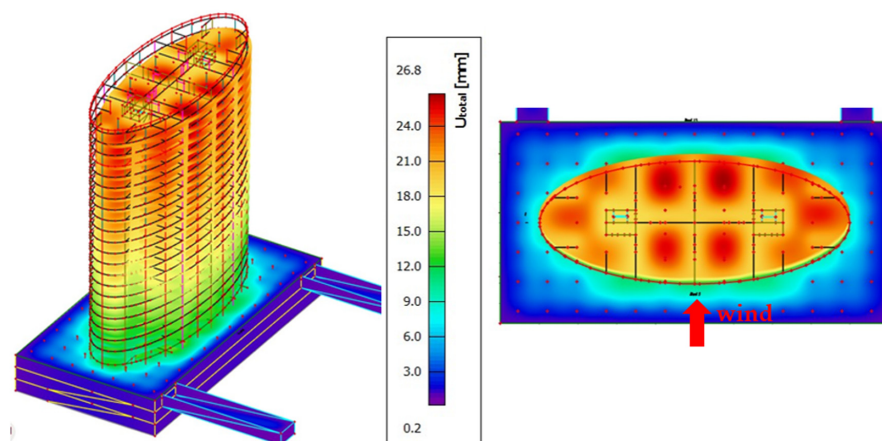


Figure 30. Three-dimensional deformation  $u_{tot}$  calculated for  $k_z = 40,421 \text{ kN/m}^3$ , wind direction  $90^\circ$ .

The influence of the wind direction and varied values of subsoil stiffness coefficients on the values of horizontal displacements in both directions is shown in Tables 6 and 7.

**Table 6.** The horizontal displacement in the x-direction (mm).

Subsoil Stiffness Coefficient (MN/m <sup>3</sup> )	Wind Direction						Limit Value (mm)
	0°		20°		90°		
25	−0.5	0.2	−3.6	−2.6	0.4	6.7	40
40.421	−0.5	0.2	−3.6	−2.9	0.4	6.1	
50	−0.5	0.1	−3.6	−2.9	0.3	5.8	
100	−0.5	0	−3.6	−3.2	0.3	5.2	

**Table 7.** The horizontal displacement in the y-direction (mm).

Subsoil Stiffness Coefficient (MN/m <sup>3</sup> )	Wind Direction						Limit Value (mm)
	0°		20°		90°		
25	−0.3	0.5	2.3	12.2	−1.4	11.0	40
40.421	−0.3	0.4	2.2	11.7	−1.4	10.4	
50	−0.4	0.4	2.2	11.5	−1.4	10.1	
100	−0.4	0.3	2.1	10.8	−1.4	9.3	

A comparison of horizontal displacements in both directions for the unfavorable wind direction of 20° is presented in Tables 8 and 9.

**Table 8.** The horizontal displacement in the x-direction (mm).

Slab No.	Structural Height	The Limit Value SH/1500	Horizontal Displacement $u_{up}$	Horizontal Displacement $u_{down}$	Difference $u_{up} - u_{down}$	Advisement
(-)	(mm)	(mm)	(mm)	(mm)	(mm)	
21	3200	2.13	2.2	2.1	0.1	satisfied
20	3200	2.13	2.1	2	0.1	satisfied
19	3200	2.13	2	1.9	0.1	satisfied
18	3200	2.13	1.9	1.8	0.1	satisfied
17	3200	2.13	1.8	1.7	0.1	satisfied
16	3200	2.13	1.7	1.6	0.1	satisfied
15	3200	2.13	1.6	1.5	0.1	satisfied
14	3200	2.13	1.5	1.4	0.1	satisfied
13	3200	2.13	1.4	1.3	0.1	satisfied
12	3200	2.13	1.3	1.2	0.1	satisfied
11	3200	2.13	1.2	1.1	0.1	satisfied
10	3200	2.13	1.1	1	0.1	satisfied
9	3200	2.13	1	0.9	0.1	satisfied
8	3200	2.13	0.9	0.8	0.1	satisfied
7	3200	2.13	0.8	0.7	0.1	satisfied
6	3200	2.13	0.7	0.6	0.1	satisfied
5	3200	2.13	0.6	0.5	0.1	satisfied
4	3200	2.13	0.5	0.3	0.2	satisfied
3	3200	2.13	0.4	0.2	0.2	satisfied
2	3200	2.13	0.3	0.1	0.2	satisfied
1	3950	2.63	0.2	0	0.2	satisfied

**Table 9.** The horizontal displacement in the y-direction (mm).

Slab No.	Structural Height	The Limit Value SH/1500	Horizontal Displacement $u_{up}$	Horizontal Displacement $u_{down}$	Difference $u_{up} - u_{down}$	Advisement
(-)	(mm)	(mm)	(mm)	(mm)	(mm)	
21	3200	2.13	11.7	11.3	0.4	satisfied
20	3200	2.13	11.3	10.9	0.4	satisfied
19	3200	2.13	10.9	10.5	0.4	satisfied
18	3200	2.13	10.5	10.1	0.4	satisfied
17	3200	2.13	10.1	9.6	0.5	satisfied
16	3200	2.13	9.6	9.1	0.5	satisfied
15	3200	2.13	9.1	8.6	0.5	satisfied
14	3200	2.13	8.6	8.1	0.5	satisfied
13	3200	2.13	8.1	7.5	0.6	satisfied
12	3200	2.13	7.5	7	0.5	satisfied
11	3200	2.13	7	6.4	0.6	satisfied
10	3200	2.13	6.4	5.8	0.6	satisfied
9	3200	2.13	5.8	5.2	0.6	satisfied
8	3200	2.13	5.2	4.6	0.6	satisfied
7	3200	2.13	4.6	4	0.6	satisfied
6	3200	2.13	4	3.4	0.6	satisfied
5	3200	2.13	3.4	2.8	0.6	satisfied
4	3200	2.13	2.8	2.2	0.6	satisfied
3	3200	2.13	2.2	1.6	0.6	satisfied
2	3200	2.13	1.6	1	0.6	satisfied
1	3950	2.63	1	0	1	satisfied

The axial force in the most loaded column was less than 8000 kN for the wind direction of 90°. For the other wind directions (0° and 20°), this value was about 100–200 kN smaller.

## 6. Discussion

External pressure coefficients were determined for varied wind directions 0°–90° (with the step 10°) using wind tunnel tests. From the comparison, it was not possible to determine which wind direction is the most dangerous for the investigated building. Therefore, resultant wind forces and maximum torsional moments were calculated. It is evident from Tables 2–4 that the wind direction of 20° caused the maximum torsional moment and the wind direction of 90° induced the maximum force (but the torsional moment was small). Therefore, both wind directions were considered (the wind direction of 0° was also taken but only for comparison) in the static analysis. The shape of the elliptical cylinder is very sensitive to the applied wind. Positive pressures are only on a small area of the windward side. The rest of the windward side is loaded by negative pressures. Therefore, torsional effects can occur, and they can be dangerous for the structure. The leeward side is completely loaded by negative pressures.

The results from the wind tunnel tests were used for the setting of the CFD simulation, which was necessary for a detailed analysis of the roof with three roof parapet alternatives (without roof parapet, with 0.5 m roof parapet, and with 2.5 m roof parapet). In the case of the wind direction of 90°, there were only negative pressures in all three alternatives. The roof parapet with a height of 2.5 m resulted in negative pressures that were half of those recorded for the alternative without a roof parapet.

In the case of the wind direction of 20°, the pressure distribution was approximately the same (with respect to the area), but the external pressure coefficients were larger in comparison with the wind direction of 0° for all three roof alternatives.

The static analysis was focused on the assessment of the horizontal displacements calculated for varied values of subsoil stiffness coefficients (25, 40, 50, 100 MN/m<sup>3</sup>), in both the x- and y-directions. In the x-direction (parallel with the major axis), a significant value was calculated only for the wind direction of 90° (5.2–6.7 mm). In the y-direction (parallel

with the minor axis), both the wind direction of 20° and the wind direction of 90° caused large values of displacements (in the ranges of 10.8–12.2 mm and 9.3–11.0 mm).

From the assessment of maximum vertical deformation, it is evident that the calculated and limit values are the same. In a real case, the vertical deformation would be less than the calculated one (because of the procedures of construction). On a real site, a geodesist adjusts the horizontal line, and the deformation incurred during the construction is reduced.

## 7. Conclusions

The shape of the investigated building is very simple—a tall elliptical cylinder. However, the presented results of the wind analysis of the shape of the structure and static analysis confirmed that the implementation of results obtained from wind tunnel tests or CFD simulations is not easy. The external pressure coefficients determined for different wind directions are very important, but they give only local information about the pressure distribution. The better procedure for the determination of the influence of wind on the structure is the calculation of resultant forces. We tried to “exclude” the wind tunnel tests and CFD simulation and to obtain the data by using the information in valid standards. The simplification of the shape by using a rectangle, a circle, or their combination did not provide suitable results. Wind tunnel tests are expensive and time-consuming, but they are the most accurate tool for the determination of the wind pressure distribution on different shapes of structures, including the case of elliptical cylinders.

**Author Contributions:** Methodology and supervision, O.I. and O.H.; formal analysis, M.F.; writing—review and editing, L.B.K.; tests in BLWT in Bratislava, L.B.K. and M.F.; CFD visualization, M.M. All authors have read and agreed to the published version of the manuscript.

**Funding:** This research was funded by the Grant Agency of the Ministry of Education, Science, Research and Sport of the Slovak Republic, grant numbers VEGA 1/0453/20 and VEGA 1/0155/23.

**Data Availability Statement:** The data used for this analysis are not available on the web page. We can cooperate with other colleagues from other universities, they can contact us thru email addresses.

**Conflicts of Interest:** The authors declare no conflict of interest. The funders had no role in the design of the study; in the collection, analyses, or interpretation of data; in the writing of the manuscript; or in the decision to publish the results.

## References

1. Cresco.sk. Available online: <https://www.cresco.sk/sk/projekty/rezidencne/detail/iii-veze/> (accessed on 12 April 2022). (In Slovak).
2. YES IN MY BRATISLAVA. Available online: <https://www.yimba.sk/narodny-futbalovy-stadion> (accessed on 12 April 2022). (In Slovak).
3. Officerentinfo.sk. Available online: <https://www.officerentinfo.sk/article/officemarket-news/which-is-the-most-beautiful-high-rise-building-in-bratislava> (accessed on 12 April 2022).
4. Merrick, R.; Bitsuamlak, G. Shape effects on the wind-induced response of high-rise buildings. *J. Wind. Eng.* **2009**, *6*, 381–390.
5. Zhao, D.-X.; He, B.-J. Effects of architectural shape on surface wind pressure distribution: Case studies of oval-shaped tall buildings. *J. Build. Eng.* **2017**, *12*, 219–228.
6. Golasz-Szolomicka, H.; Szolomicky, J. Architectural and structural analysis of selected twisted tall buildings. *Mater. Sci. Eng.* **2019**, *471*, 052050. [[CrossRef](#)]
7. Choi, J.H.; Lee, S.J. Ground effect of flow around an elliptic cylinder in a turbulent boundary layer. *J. Fluids Struct.* **2000**, *14*, 697–709. [[CrossRef](#)]
8. Daichin Lee, S.J. Flow structure of the wake behind an elliptic cylinder close to a free surface. *KSME Int. J.* **2011**, *15*, 1784–1793. [[CrossRef](#)]
9. Modi, V.; Wiland, E. *Unsteady Aerodynamics of Stationary Elliptic Cylinders in Subcritical Flow*; The University of British Columbia: Vancouver, BC, Canada, 2012. [[CrossRef](#)]
10. Shintani, K.; Umemura, A.; Takano, A. Low-Reynolds-number flow past an elliptic cylinder. *J. Fluid Mech.* **1983**, *136*, 277–289. [[CrossRef](#)]
11. Johnson, S.A.; Thompson, M.C.; Hourigan, K. Predicted low frequency structures in the wake of elliptical cylinders. *Eur. J. Mech. B/Fluid.* **2004**, *23*, 229–239. [[CrossRef](#)]
12. Thompson, M.C.; Radi, A.; Rao, A.; Sheridan, J.; Hourigan, K. Low-Reynolds-number wakes of elliptical cylinders: From the circular cylinder to the normal flat plate. *J. Fluid Mech.* **2014**, *751*, 570–600. [[CrossRef](#)]

13. Takeuchi, T.; Maeda, J. Unsteady wind force on an elliptic cylinder subjected to a short-rise-time gust from steady flow. *J. Wind Eng. Ind. Aerod.* **2013**, *122*, 138–145. [[CrossRef](#)]
14. Sheared, G.J. Cylinders with Elliptic Cross-Section: Wake Stability with Variation in Angle of Incidence. 2007. Available online: [https://sheardlab.org/assets/Sheard\\_iutam2007.pdf](https://sheardlab.org/assets/Sheard_iutam2007.pdf) (accessed on 14 April 2022).
15. Jafari, M.; Alipour, A. Aerodynamic shape optimization of rectangular and elliptical double-skin facades to mitigate wind-induced effects on tall buildings. *J. Wind Eng. Ind. Aerod.* **2021**, *213*, 104586. [[CrossRef](#)]
16. Shi, X.; Alam, M.; Bai, H. Wakes of elliptical cylinders at low Reynolds number. *Int. J. Heat Fluid Flow* **2020**, *82*, 108553.
17. Meleka, N.; Hekal, G.; Rizk, A. Comparative study on static and dynamic analysis of structures. *Eng. Res. J.* **2016**, *39*, 277–283. Available online: [https://erjm.journals.ekb.eg/article\\_66395\\_519e40b715e2db7ef633797cde5338b9.pdf](https://erjm.journals.ekb.eg/article_66395_519e40b715e2db7ef633797cde5338b9.pdf) (accessed on 18 April 2022).
18. STN EN 1992-1-1 Eurocode 2; Design of Concrete Structures. Part 1: General Rules and Rules for Buildings. CEN: Brussels, Belgium, 2004.
19. STN EN 1998-1 Eurocode 8; Design of Structures for Earthquake Resistance. Part 1: General Rules, Seismic Actions and Rules for Buildings. CEN: Brussels, Belgium, 2005.
20. STN EN 1991-1-4 Eurocode 1; Actions on Structures. Part 1-4: General Actions. Wind Actions. CEN: Brussels, Belgium, 2007.
21. STN EN 1991-1-4/NA Eurocode 1; Actions on Structures. Part 1-4: General Actions. Wind Actions. National Annex. CEN: Brussels, Belgium, 2007. (In Slovak)
22. Hubová, O.; Konečná, L.; Lobotka, P. Determination of the Most Suitable Place in Cross-Section of BLWT Tunnel for Calibration of Measuring Devices. In Proceedings of the 6th International Scientific Conference Dynamics of Civil Engineering and Transport Structures and Wind Engineering DYN-WIND, Žilina, Slovakia, 26–29 May 2014; pp. 86–89.
23. Franek, M.; Konečná, L.; Hubová, O.; Žilinský, J. Experimental pressure measurement on elliptic cylinder. *Appl. Mech. Mater.* **2016**, *820*, 332–337. [[CrossRef](#)]
24. Bearman, P.W. On vortex shedding from a circular cylinder in the critical Reynolds number regime. *J. Fluid Mech.* **1969**, *37*, 577–585. [[CrossRef](#)]
25. Gu, Z.F.; Sun, T.F. On interference between two circular cylinders in staggered arrangement at high subcritical Reynolds numbers. *J. Wind Eng. Ind. Aerod.* **1999**, *80*, 287–309. [[CrossRef](#)]
26. Wu, G.; Du, X.; Wang, Y. LES of flow around two staggered circular cylinders at a high subcritical Reynolds number of  $1.4 \times 10^5$ . *J. Wind Eng. Ind. Aerod.* **2020**, *196*, 104044. [[CrossRef](#)]
27. Franek, M.; Macák, M.; Žilinský, J. CFD evaluation of boundary layer and wind loads on elliptic cylinder. In Proceedings of the 4th International Conference on Applied Technology—ATF, Leuven, Belgium, 15–17 September 2016; pp. 112–117, ISBN 9789086497966.
28. STN EN 1991-1-1 Eurocode 1; Actions on Structures. Part 1-1: General Actions. Densities, Self-Weight, Imposed Loads for Buildings. CEN: Brussels, Belgium, 2007.
29. STN EN 1991-1-1/NA Eurocode 1; Actions on Structures. Part 1-1: General Actions. Densities, Self-Weight, Imposed Loads for Buildings. National Annex. CEN: Brussels, Belgium, 2004.
30. STN EN 1991-1-3 Eurocode 1; Actions on Structures. Part 1-1: General Actions. Snow Loads. CEN: Brussels, Belgium, 2007.
31. STN EN 1991-1-3/NA1 Eurocode 1; Actions on Structures. Part 1-1: General Actions. Snow Loads. National Annex. CEN: Brussels, Belgium, 2007.
32. Jendželovský, N. *The Modelling of Foundations by Finite Element Method*, 1st ed.; STU Publishing House: Bratislava, Slovakia, 2009. (In Slovak)
33. Frankovská, J.; Súľovská, M.; Turček, P. *The Foundation of Structures. Background Papers for Design of Foundations*, 1st ed.; STU Publishing House: Bratislava, Slovakia, 2011. (In Slovak)
34. Turček, P.; Hulla, J. *The Foundation of Structures*, 2nd ed.; Jaga Group: Bratislava, Slovakia, 2004. (In Slovak)
35. STN EN 1997-1 Eurocode 7; Geotechnical Desing. Part 1: General Rules. CEN: Brussels, Belgium, 2005.
36. Harvan, I. Resistance of the Tall and Super-Tall Building on the Wind Effects and Effects of Earthquakes. ABS, 2011. Available online: <https://www.asb.sk/stavebnictvo/odolnost-vysokych-asupervysokych-budov-proti-ucinkom-vetra-azemetraseni> (accessed on 20 May 2022). (In Slovak).

**Disclaimer/Publisher’s Note:** The statements, opinions and data contained in all publications are solely those of the individual author(s) and contributor(s) and not of MDPI and/or the editor(s). MDPI and/or the editor(s) disclaim responsibility for any injury to people or property resulting from any ideas, methods, instructions or products referred to in the content.